

# Iron's impact on silicon solar cell execution: comprehensive modeling across diverse scenarios

Oleg Olikh\*, Oleksii Zavhorodnii

Taras Shevchenko National University of Kyiv, 64/13, Volodymyrska Street, Kyiv, 01601, Ukraine

---

## ARTICLE INFO

**Keywords:**  
silicon  
iron–boron pairs  
solar cells  
SCAPS simulation  
defect influence  
estimation of iron contamination

---

## ABSTRACT

Silicon solar cells are vital for renewable energy but often degrade from iron-induced carrier recombination. This study investigates the impact of iron-related defect variability on the photovoltaic performance of  $n^+ - p$  structure through comprehensive SCAPS simulations and experimental measurements. The effect of iron–boron pair dissociation on silicon solar cell (SSC) short-circuit current, open-circuit voltage, fill factor, and efficiency was analyzed under diverse conditions. Simulations covered temperatures (290–340 K), iron concentrations ( $10^{10}$ – $10^{14}$  cm $^{-3}$ ), and SSC base thicknesses (180–380  $\mu\text{m}$ ) and boron doping ( $10^{15}$ – $10^{17}$  cm $^{-3}$ ) under AM1.5 and monochromatic (940 nm) illumination. Experimental results confirmed simulation predictions. The study assessed the ability to use photoelectric parameter variations for iron quantification, identifying short-circuit current under monochromatic light as a highly reliable metric. The study correlations between photoelectric characteristics suggested that Principal Component Analysis is advisable for dimensionality reduction when SSC multiple parameters are used in non-invasive iron detection.

---

## 1. Introduction

The necessity for renewable energy sources to meet the growing global demand for sustainable and environmentally friendly energy alternatives has become evident. Among the wide range of renewable energy sources, sunlight is the cleanest, safest, and most abundant source for use in sustainable energy to support economic growth [1]. The utilization of solar energy heavily depends on the use of photovoltaic cells. The development of next-generation solar cells is primarily driven by the search for novel materials suitable for their fabrication. Particular attention is given to exploring the potential use of composites and nanoparticles (e.g., Cu-La-based systems [2], cerium oxide, and copper indium sulfate [3]), MAX phases [4, 5], and chalcogenides (such as GeSe, MoSe<sub>2</sub>, Sb<sub>2</sub>Se<sub>3</sub>, and SnSe as hole transport materials [6] or SnS<sub>2</sub> and WS<sub>2</sub> as electron transport materials [7]), as well as metal silicides (e.g., FeSi<sub>2</sub> as an absorber layer [8]). These studies cover a broad range of materials [9], with the primary goal of developing highly efficient and cost-effective photovoltaic devices. Frequently, these novel materials are integrated with silicon in solar cells [8, 10]. However, it is worth noting that traditional silicon-based devices continue to play a dominant role in the photovoltaic market [11, 12].

The issue of semiconductor purity has become increasingly significant since the advent of the transistor in 1947 [13]. The 1960 study by Shockley and Queisser [14] demonstrated that the electrical properties of  $n^+ - p$  silicon diodes deteriorate when impurity atoms of metals such as Cu, Fe, Mn, Au, Zn, and Ni are present. As a result, investigations were initiated to prevent metal contamination in semiconductors during manufacturing. In particular, metallic impurities are known to reduce the efficiency of silicon-based devices through direct shunting [15], increased leakage current [16], or bulk recombination [17]. Despite extensive study of metallic impurities in silicon over the past fifty years [13, 18], the problem continues to attract significant attention [19, 20, 21, 22, 23].

Iron is prominent among metallic contaminants, with its atoms being among the most prevalent and detrimental impurities in silicon solar cells (SSCs) [24]. The main sources of iron contamination in monocrystalline SSCs include [17, 25] cleaning processes (due to residual impurities in chemicals), annealing and oxidation (from furnaces in general and heating coils in particular), equipment utilizing plasma and ions (e.g., ion implantation, dry etching, resist ashing, sputtering), wafer handling and transportation (despite the widespread use of plastic rather than metal components). Even in small concentrations (about  $10^{10}$  cm $^{-3}$ ), point defects related to Fe can significantly influence the performance of SSCs [26, 27]. Therefore, it is of critical importance to assess the concentration of iron impurities. In response to

---

\* olegolikh@knu.ua (O. Olikh); nevermor464@gmail.com (O. Zavhorodnii)  
ORCID(s): 0000-0003-0633-5429 (O. Olikh); 0000-0001-8080-7661 (O. Zavhorodnii)

this challenge, various methodologies have been put forward, often based on the property of iron atoms to form pairs with acceptors. In particular, iron atoms are predominantly located in interstitial positions in silicon, forming the  $\text{Fe}_i$  defect. In *p*-type crystals, without external illumination, iron atoms carry positive charges and tend to bond with negatively charged doping atoms (boron, aluminum, gallium, or indium), forming  $\text{Fe}_i\text{B}_{\text{Si}}$  pairs [28]. However, these pairs can destabilize by intense illumination, electron injection, or heating up to 200 °C [29]. The recombination properties of iron-related defects  $\text{Fe}_i$  and  $\text{Fe}_i\text{B}_s$  differ significantly, which profoundly affects the overall characteristics of the crystal. This fact formed the basis for the first method of assessing iron concentration [30], which relied on measuring the diffusion length of minority carriers using the surface photovoltage method [31]. Many other methods involve measurements of carrier lifetime [32, 33], Quasi-Steady-State Photoconductance [34], or the study of kinetic dependencies of short-circuit current [35] or photoluminescence intensity [36] during the reaction  $\text{Fe}_i\text{B}_{\text{Si}} \rightleftharpoons \text{Fe}_i + \text{B}_{\text{Si}}$ .

Notably, the presence of Fe-related defects affects the dynamics of electron and hole movement within the solar cell, which is reflected in changes to the appearance of the current–voltage (*I*–*V*) characteristics of SSCs overall, as well as modifications to the main photoelectric parameters (short-circuit current  $I_{\text{SC}}$ , open-circuit voltage  $V_{\text{OC}}$ , efficiency  $\eta$ , and fill factor  $FF$ ) in particular. These findings create fundamental possibilities to advance methods for estimating iron concentration by *I*–*V* curves measuring before and after pair dissolution. The advantages of such an approach are associated with the possibility of directly characterizing finished solar cells, as well as the absence of the need for additional equipment other than that required for *I*–*V* measurements, which is extremely common. Efforts have been made initially in developing such methods. For instance, it was proposed to estimate the concentration of iron in SSCs based on changes in the ideality factor [37, 38] or open-circuit voltage [27]. However, developing such approaches requires evaluating how a particular parameter changes when iron-containing pairs dissolve and determining whether it can estimate the iron concentration  $N_{\text{Fe}}$ . For example, the most evident conditions for utilizing a specific parameter include its change due to the transformation  $\text{Fe}_i\text{B}_{\text{Si}} \rightarrow \text{Fe}_i + \text{B}_{\text{Si}}$ , at least by 10 %, along with a monotonic dependence of these changes on  $N_{\text{Fe}}$ .

This paper intends to determine the variations of  $I_{\text{SC}}$ ,  $V_{\text{OC}}$ ,  $\eta$ , and  $FF$  resulting from the decay of iron-containing pairs in boron-doped silicon solar cells. Previous similar calculations have been conducted [39, 26, 19], but the results presented typically pertain only to certain temperatures, illumination levels (often AM1.5), and solar cells with specific parameters. In this study, we performed calculations over a sufficiently wide temperature range (290–340 K) and for solar cells with varying base thickness (180–380 μm) and doping levels (boron concentration in the base ranging from  $10^{15}$  to  $10^{17}$  cm<sup>−3</sup>). The obtained results enable us to evaluate the feasibility and potential of using the main photovoltaic parameters of silicon solar cells to estimate the  $N_{\text{Fe}}$  value across a temperature range close to operating conditions. Furthermore, investigations have explored changes in photoelectric performance under not only solar illumination (AM1.5G) but also low-intensity monochromatic light (wavelength of 940 nm, intensities of 5 W/m<sup>2</sup> and 10 W/m<sup>2</sup>). In the first case, while it is customary to adhere to standard conditions, it's essential to consider that illumination at 1000 W/m<sup>2</sup> can lead to the decay of  $\text{Fe}_i\text{B}_s$  complexes [40]. Therefore, measurements for cases requiring the presence of undissociated pairs in silicon must meet specific constraints. On the other hand, intentionally chosen monochromatic illumination penetrates the emitter with negligible losses and does not reach the rear side. In this context, the photoelectric parameters show remarkable sensitivity to recombination processes occurring within the solar cell base and to iron concentration in this region. Finally, in our calculations, we attempted to use the latest literature data concerning the exact values of silicon parameters, including light absorption values [41] and coefficients characterizing intrinsic recombination [42, 43].

The contributions of this work are as follows:

- The impact of FeB pair dissociation on the short-circuit current, open-circuit voltage, fill factor, and efficiency of silicon solar cells was investigated through simulation. Calculations were performed over various temperatures, illumination conditions, and solar cell parameters, including base thickness, doping level, and impurity concentration. Particular attention was given to the silicon and defect parameters value under diverse conditions.
- A series of experiments have been done to check the simulation predictions.
- The feasibility of using variations in short-circuit current, open-circuit voltage, fill factor, and efficiency due to impurity pair dissociation for iron concentration estimation was analyzed, and the most reliable parameter — short-circuit current under monochromatic illumination — was identified.
- The potential of simultaneous using multiple photovoltaic parameters for iron quantification, including machine learning techniques, was explored. It was shown that applying Principal Component Analysis as a preprocessing step is beneficial in this case.

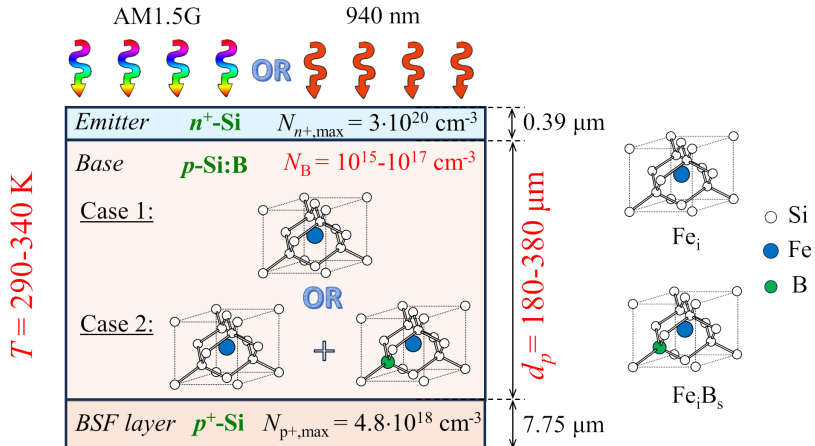


**Figure 1:** Schematic diagram of analysed solar cell. The figure also presents the solar cell parameters and external conditions that varied during the simulation — see the main text for details. The right side of the figure illustrates the configurations of interstitial iron  $\text{Fe}_i$  and iron-boron pairs  $\text{Fe}_i\text{B}_s$ .

**Table 1**

Parameters varied during the simulation

Parameter	Range of values
$d_p (\mu\text{m})$	180 – 380
$N_B (\text{cm}^{-3})$	$10^{15} - 10^{17}$
$N_{\text{Fe}} (\text{cm}^{-3})$	$10^{10} - 10^{14}$
$T (\text{K})$	290 – 340
Illumination	AM1.5G, 1000 $\text{W/m}^2$ ; 940 nm, 5 $\text{W/m}^2$ ; 940 nm, 10 $\text{W/m}^2$

## 2. Research Methodology

### 2.1. Simulation Details

The study involved simulation  $I$ - $V$  curves of SSCs with an  $n^+$ - $p$ - $p^+$  structure, as illustrated in Fig. 1. A back surface field (BSF,  $p^+$ -layer) is a notable feature observed in both Al-BSF cells (full area), which are gradually losing relevance, and PERC cells (locally), which are the most widely used in mass production. The structures with a base uniformly doped with boron were under consideration. The doping concentration  $N_B$ , and the base thickness  $d_p$  were varied during the modeling process, as detailed in Table 1. The emitter and  $p^+$ -layer were considered to be unevenly doped. The concentration profiles of the dopants, their maximum values ( $N_{p^+,max}$  and  $N_{n^+,max}$ ), and layer thicknesses (see Fig. 1) were selected according to Fell et al. [44].

The simulation was conducted using the SCAPS 3.3.11 code [45]. SCAPS-1D software, developed by the University of Gent, is founded on theoretical computations that involve solving Poisson's equation, continuity equations for holes and electrons, and drift-diffusion at each position within the solar cell, considering the boundary conditions. Despite its one-dimensional modeling approach, SCAPS is extensively used for modeling various types of solar cells [6, 7, 8, 46, 47, 48, 49] in general and for investigating the effects of defects on their performance [6, 8, 50, 51, 52] in particular.

As can be seen from Table 1, calculations spanned a broad range of temperatures and base doping levels. Therefore, to improve the accuracy of the calculations when inputting the initial parameters into SCAPS, temperature and concentration (where applicable) dependencies of the following silicon parameters were taken into account:

- bandgap according to Passler [53];
- doping induced bandgap narrowing according to Yan & Cuevas [54];

- effective density of states at conduction and valence band and intrinsic carrier concentration according to Couderc et al. [55];
- thermal carrier velocities according to Green [56];
- free carrier effective masses according to O'Mara et al. [57];
- carrier mobilities according to Klaassen's theory [58];

The values of surface recombination coefficients were considered equal to the thermal velocities of carriers [44]. The calculations addressed recombination processes within the structural volume, incorporating both intrinsic recombination and Shockley-Read-Hall (SRH) recombination at iron-related defects. In the first case, processes of band-to-band radiation recombination were considered (where the calculation of the corresponding coefficient included the fraction of radiatively emitted photons reabsorbed via band-to-band processes according to Niewelt et al.[42]) and Auger recombination (where the coefficients considered the effect of Coulomb enhancement [43] and temperature dependence [59]).

When accounting for the influence of iron impurities, we considered that Fe atoms were uniformly distributed within the base and  $p^+$ -layer with a total concentration of  $N_{\text{Fe}}$  (see Table 1). Two cases were under consideration:

Case 1. The concentration of interstitial iron defects  $[\text{Fe}_i] = N_{\text{Fe}}$  at each position throughout the solar cell, with no pairs present  $[\text{Fe}_i\text{B}_s] = 0$ . This case corresponds to the state of the structure immediately after intense illumination, for example.

Case 2. Iron atoms predominantly form pairs with acceptors,  $[\text{Fe}_i\text{B}_s] \gg [\text{Fe}_i]$ , but the exact concentration ratio depends on the position of the Fermi level and temperature [60, 61] and varies from point to point within the solar cell. Further details about calculation of the concentration profiles of  $\text{Fe}_i\text{B}_s$  and  $\text{Fe}_i$  are provided in [38, 37]. This case corresponds to prolonged storage of the structure in darkness or under conditions of low-intensity ( $< 0.01 \text{ J cm}^{-2}$  [40]) illumination.

During the calculations, it was assumed that  $\text{Fe}_i$  forms a single donor level, while the  $\text{Fe}_i\text{B}_s$  pair has a trigonal configuration and acts as an amphoteric defect. We obtained defect parameters, including energy level positions within the bandgap, electron and hole capture cross-sections, and their temperature dependencies, based on data from relevant studies [62, 63, 64].

As previously mentioned, the solar cell behavior was simulated under different illumination conditions, including solar light (AM1.5G) and monochromatic light (wavelength 940 nm, intensity of  $W_{\text{ill}} = 5 \text{ W/m}^2$  or  $10 \text{ W/m}^2$ ) — see Table 1. The calculations incorporated the light absorption values in silicon based on Green's study [41].

The  $I$ - $V$  characteristics were simulated for both Case 1 and Case 2 (see Fig. 2), and from each curve, the short-circuit current, open-circuit voltage, efficiency, and fill factor were determined. Assessing the influence of iron defect variability relied on the relative changes in each photovoltaic conversion parameter:

$$\varepsilon A = \frac{A^{\text{FeB}} - A^{\text{Fe}}}{A^{\text{FeB}}} \times 100\%, \quad (1)$$

where  $A$  represents one of the parameters ( $I_{\text{SC}}$ ,  $V_{\text{OC}}$ ,  $\eta$ , and  $FF$ ), superscript "FeB" corresponds to the parameter value for coexistence of  $\text{Fe}_i$  and  $\text{Fe}_i\text{B}_s$  (Case 2), superscript "Fe" is related to the decay of all pairs (Case 1).

Impact of change of iron defects was investigated as a function of temperature from 290 K to 340 K, base depth from 180  $\mu\text{m}$  to 380  $\mu\text{m}$ , base doping level from  $10^{15} \text{ cm}^{-3}$  to  $10^{17} \text{ cm}^{-3}$ , and total impurity iron atom concentration from  $10^{10} \text{ cm}^{-3}$  to  $10^{14} \text{ cm}^{-3}$ . It is worth noting that investigating the effects of doping density, defect density, temperature, and active layer thickness on photovoltaic parameters is a well-established practice [6, 7, 8]. For each illumination scenario, calculations were carried out with 11 different temperature values and 5 base depth values, evenly distributed within the specified ranges. The concentration values were distributed equally on a logarithmic scale with 4 ( $N_B$  case) and 6 ( $N_{\text{Fe}}$  case) steps per decade. As a result, for the AM1.5 illumination scenario, for instance, 24750  $I$ - $V$  characteristics were simulated. An exception occurred with monochromatic illumination at  $W_{\text{ill}} = 10 \text{ W/m}^2$ , where we used only two  $d_p$  values.

In general, interstitial iron is already mobile at room temperature and can interact with various impurities. Over 30 iron-related complexes have been identified in silicon, and nearly 25 energy levels associated with iron-related defects have been reported in the silicon bandgap across different studies [63, 65, 66]. For example, iron forms complexes with carbon, oxygen, hydrogen, sulfur, and other metal impurities, as well as with native defects in silicon. However, in terms of their impact on photovoltaic performance, two primary factors must be considered. First, the concentration

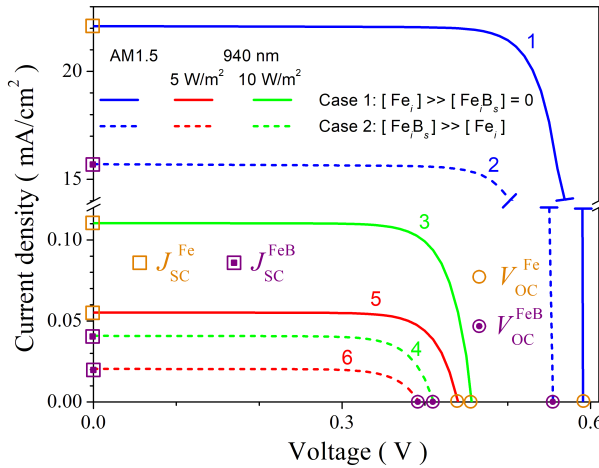


**Figure 2:** Typical IV characteristics, calculated for structure with  $d_p = 180 \mu\text{m}$ ,  $N_B = 10^{17} \text{ cm}^{-3}$ ,  $N_{\text{Fe}} = 10^{14} \text{ cm}^{-3}$  at  $T = 290 \text{ K}$ . Illumination: AM1.5 (curves 1, 2), 940 nm 10 W/m<sup>2</sup> (3, 4) and 940 nm 5 W/m<sup>2</sup> (5, 6). Solid (1, 3, 5) and dotted (2, 4, 6) lines correspond to Case 1 and Case 2, respectively. The figure also indicates the short-circuit current values (squares) and open-circuit voltage values (circles) for two scenarios: the dissociation of all pairs (empty marks), and the coexistence of  $\text{Fe}_i$  and  $\text{Fe}_i\text{B}_s$  (marks with a dot inside).

of the relevant defects is crucial. It is widely recognized that in *p*-type silicon under equilibrium conditions, most iron impurity atoms pair with acceptors (e.g., boron in Si:B) [28, 63]. The concentration of other complexes is significantly lower, and detailed investigation of these complexes requires specialized sample preparation, such as additional doping with other expected complex components or irradiation to increase the concentration of native defects [67]. Further supporting this, several methods used to evaluate the total iron concentration in *p*-Si rely on breaking the FeB pair [30, 36, 35]. Second, the recombination activity of these centers must be considered, as it depends on the defect energy level relative to the Fermi level and the charge carrier capture cross-section. Interstitial iron and FeB pairs are among the most detrimental recombination-active impurities in *p*-Si [63, 68] in contrast to other iron-related defects. Notably, iron gettering by oxygen precipitates or structural defects increases carrier lifetime [69, 70]. In *n*-Si,  $\text{Fe}_i$  is not a recombination-active impurity due to the filling of its energy level. Reducing the impact of iron through gettering during phosphorus diffusion [69, 70, 71] or the formation of a passivating layer [72] is well-established and used in the solar cell industry.

Thus, our assumption that the primary influence of iron impurities in the *p*-regions of a solar cell on photoelectric parameters is due to  $\text{Fe}_i\text{B}_{\text{Si}}$  pairs and  $\text{Fe}_i$  is fully justified. Furthermore, we emphasize that this paper focuses on the relative changes in parameters during  $\text{Fe}_i\text{B}_{\text{Si}} \rightleftharpoons \text{Fe}_i + \text{B}_{\text{Si}}$  transformation, which enables the isolation of these specific defects' contributions.

## 2.2. Experimental Details

To evaluate the validity of the simulated results, we also conducted experimental studies on the effect of changing the state of iron-related defects on the photoelectric parameters of silicon solar cells.

The  $n^+ \text{-} p^+ \text{-} \text{Si}$  samples were used in the experiment. The structure was fabricated from a 380  $\mu\text{m}$  thick *p*-type boron-doped Czochralski silicon (100) wafer with doping level  $N_B = 1.36 \times 10^{15} \text{ cm}^{-3}$ . The  $n^+$  emitter with a sheet resistance of about 20–30  $\Omega/\square$  and thickness of 0.7  $\mu\text{m}$  was formed by phosphorus diffusion. The anti-recombination isotype barrier was created by using a  $p^+$  layer (10–20  $\Omega/\square$ ) formed by boron diffusion. On the front surface,  $\text{SiO}_2$  (40 nm) and  $\text{Si}_3\text{N}_4$  (30 nm) films were formed as antireflective and passivating layers, respectively. The solid and grid Al contacts were formed by magnetron sputtering on the back and front surfaces, respectively.

The *I*-*V* characteristics were measured using a Keithley 2450 source meter and low-intensity monochromatic light source (light-emitting diode SN-HPIR940nm-1W with light wavelength 940 nm and intensity of about  $W_{\text{ill}} = 5 \text{ W/m}^2$ ).

For different samples, the iron concentration ranged from  $2 \times 10^{11}$  to  $4 \times 10^{13} \text{ cm}^{-3}$ . The values of  $N_{\text{Fe}}$  were determined using a methodology [73, 35], based on fitting the kinetics of short-circuit current. The decay of  $\text{Fe}_i\text{B}_s$  pairs was realized using intensive ( $7000 \text{ W/m}^2$ ) halogen lamp illumination.

The measurements were carried over the temperature range of 300–340 K. The sample temperature was driven by a thermoelectric cooler controlled by an STS-21 sensor and maintained constant by a PID algorithm embedded in the software that serves the experimental setup. Notably, the characteristic time for FeB pair recovery after the cessation of illumination is approximately 13,000 seconds at 300 K and only 600 seconds at 340 K [29, 74]. These limitations affect the measurement duration at high temperatures, and the experiments accounted for them.

### 3. Results and Discussion

#### 3.1. Short-circuit current

Figure 3 illustrates the characteristic dependencies of short-circuit current variations resulting from the reconfiguration of iron-containing defects, as obtained from the simulations. We present a more comprehensive set of figures that depict the detailed dependencies of  $\varepsilon I_{\text{SC}}$  on all parameters varied during the calculations in the Supplementary Material (Figs. S1–S6). It is important to note that the qualitative nature of the short-circuit current variations remains practically identical under both solar and monochromatic illumination, with the quantitative parameters of  $\varepsilon I_{\text{SC}}$  differing: at 940 nm, the absolute values of  $\varepsilon I_{\text{SC}}$  are approximately 3–4 times greater than those observed under AM1.5 conditions, assuming other parameters are constant. Among other features of  $\varepsilon I_{\text{SC}}$  changes, we can highlight the following:

- The module  $\varepsilon I_{\text{SC}}$  increases monotonically with increasing iron concentration, but the sign of this value depends on the doping level. At low boron concentrations ( $N_B = 10^{15} \text{ cm}^{-3}$ )  $\varepsilon I_{\text{SC}} > 0$ , whereas at high concentrations ( $N_B = 10^{17} \text{ cm}^{-3}$ )  $\varepsilon I_{\text{SC}} < 0$  — see Figs. 3a, 3c, S3–S6;
- Increasing the acceptor concentration causes a monotonic decrease in  $\varepsilon I_{\text{SC}}$  (Figs. 3b, 3d); the  $N_B$  value at which the sign of  $\varepsilon I_{\text{SC}}$  changes depends on the temperature (decreases with decreasing in  $T$  value) and the type of illumination (is generally higher in the case of monochromatic light) — see Fig. S2;
- In the case where  $\varepsilon I_{\text{SC}} < 0$ , an temperature increase causes a decrease in the absolute magnitude of the relative changes in short-circuit current, with the dependence being nearly linear and the slope increasing with higher doping levels and iron concentration (Figs. 3a, 3c, S4). In the case where  $\varepsilon I_{\text{SC}} > 0$ , a  $T$  changing results in minor non-monotonic variations of the short-circuit current after the dissociation of  $\text{Fe}_i\text{B}_s$  pairs (Fig. S3);
- The influence of base thickness on  $\varepsilon I_{\text{SC}}$  increases with increasing  $N_B$  and decreasing  $N_{\text{Fe}}$  (Figs. S5, S3), but it is minimal overall. As calculations have shown, increasing  $d_p$  by more than twice causes changes in  $\varepsilon I_{\text{SC}}$  that do not exceed 0.5 %;
- Changing the intensity of the monochromatic illumination (from  $5 \text{ W/m}^2$  to  $10 \text{ W/m}^2$ ) does not practically change the value of  $\varepsilon I_{\text{SC}}$ ;
- The absolute values of  $\varepsilon I_{\text{SC}}$  can reach relatively high values (more than 100 % for 940 nm illumination); however, in cases where  $N_{\text{Fe}} < 10^{11} \text{ cm}^{-3}$  and around  $N_B = 10^{16} \text{ cm}^{-3}$ , the changes in short-circuit current do not exceed a few percent.

The identified features of the  $\varepsilon I_{\text{SC}}$  changes can be explained by considering the main reasons for the influence of factors, which varied during simulation, on the photovoltaic conversion. It is known [75] that the main influence of metal impurities on solar cell performance is caused by their effect on the collection efficiency (CE, portion of excess carriers that reach the depletion region of  $p$ – $n$  junction). Neglecting the influence of series and shunt resistances, the short-circuit current coincides with the photocurrent  $I_{\text{ph}}$ , which equals the CE multiplied by the number of light-induced excess carriers. In turn, the CE can be calculated as a convolution of generation function, which is proportional to  $\exp(-\alpha z)$  (where  $\alpha$  is the absorption coefficient and  $z$  is the coordinate along the axis directed perpendicular to the  $p$ – $n$  junction from the emitter) and the collection probability, which can be obtained as a solution of homogeneous diffusion equation.

The photogenerated current for the cell can be obtained by adding the relevant quantities for the base  $I_{\text{ph},b}$  and the emitter  $I_{\text{ph},e}$  [76]:

$$I_{\text{SC}} \approx I_{\text{ph}} = I_{\text{ph},e} + I_{\text{ph},b}. \quad (2)$$

However, considering the location of the impurity iron, it can be assumed that during the  $\text{Fe}_i\text{B}_{\text{Si}} \rightleftharpoons \text{Fe}_i + \text{B}_{\text{Si}}$  reconfiguration, the first term on the right-hand side of Eq. (2) remains unchanged ( $I_{\text{ph},e}^{\text{FeB}} = I_{\text{ph},e}^{\text{Fe}} = I_{\text{ph},e}$ ), and therefore,

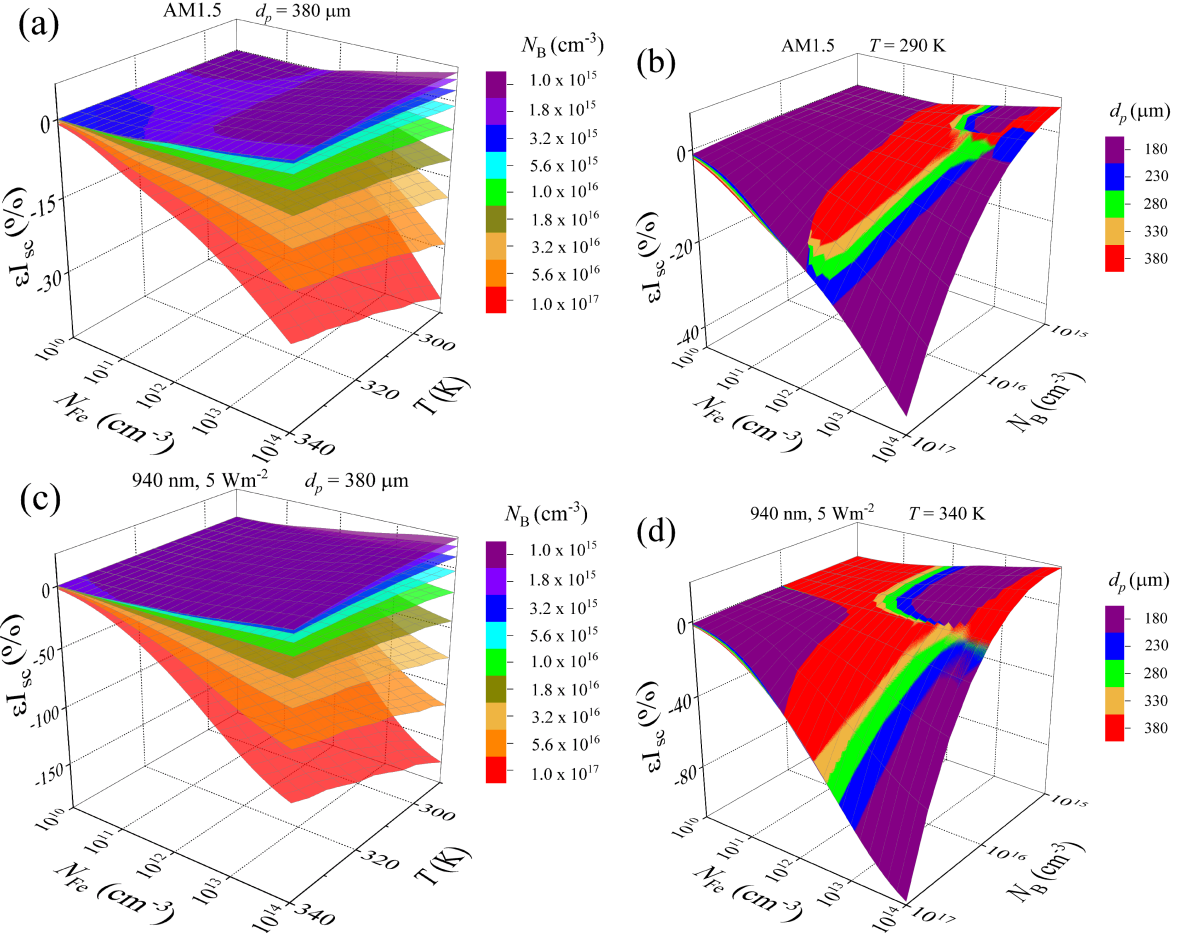


**Figure 3:** Relative changes in short-circuit current caused by a complete dissociation of  $\text{Fe}_i\text{B}_s$  pairs as a function of iron concentration and temperature (panels a and c) or doping level (b, d). Illumination: AM1.5 (a, b), 940 nm  $5 \text{ W m}^{-2}$  (c, d).  $T, \text{ K}$ : 290 (b), 340 (d). Different surfaces correspond to different doping levels (a, c) and base depths (b, d).

considering Eq. (1):

$$\varepsilon I_{\text{SC}} = \frac{I_{\text{ph,b}}^{\text{FeB}} - I_{\text{ph,b}}^{\text{Fe}}}{I_{\text{ph,e}} + I_{\text{ph,b}}^{\text{FeB}}} \times 100\%. \quad (3)$$

In turn, the base photocurrent under monochromatic illumination can be expressed as follows [77]:

$$I_{\text{ph,b}} = \frac{qF(1-R)\alpha L_n}{\alpha^2 L_n^2 - 1} \left( \alpha L_n - \frac{\frac{SL_n}{D_n} \left[ \cosh\left(\frac{d^*}{L_n}\right) - \exp(-\alpha d^*) \right] + \sinh\left(\frac{d^*}{L_n}\right) + \alpha L_n \exp(-\alpha d^*)}{\frac{SL_n}{D_n} \sinh\left(\frac{d^*}{L_n}\right) + \cosh\left(\frac{d^*}{L_n}\right)} \right), \quad (4)$$

where  $F$  is the photon flux,  $R$  is the reflection coefficient,  $S$  is the surface recombination velocity,  $L_n$  is the minority carrier (electron) diffusion length,  $D_n$  is the electron diffusion coefficient,  $d^*$  is the thickness of the quasi-neutral region base, since the space charge region (SCR) width for the modeled structures did not exceed  $1 \mu\text{m}$ , it follows that  $d^* \simeq d_p$ .

The recombination rate affects the value of  $L_n$  and, according to the SRH model, depends on trap concentrations, capture cross-sections of electrons and holes, temperature, the Fermi level  $E_F$  location, and defect levels. Temperature also affects the values of  $\alpha$  and  $D_n$ . In turn, the position of  $E_F$  within the band gap depends on temperature and doping level. Fig. 4 shows the calculated by using SCAPS temperature and concentration dependence of the Fermi

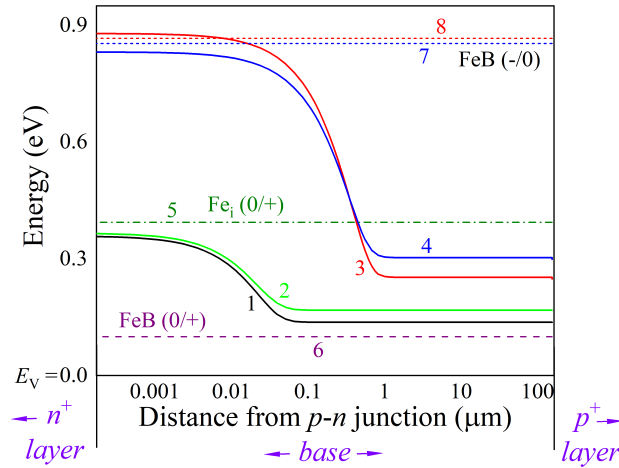


**Figure 4:** The location of the Fermi level (curves 1–4) in the base of the  $n^+$ - $p$ - $p^+$  structure as a function of distance from  $p$ - $n$  junction. The zero energy value corresponds to the top of the valence band. Also shown are the locations of the donor ( $0/+$ ) levels for the interstitial iron atom  $Fe_i$  (5) and the FeB pair (6) and the acceptor ( $-/0$ ) level for the FeB pair (7, 8).  $T, K: 290$  (1, 3, 8),  $340$  (2, 4, 7).  $N_B, \text{ cm}^{-3}: 10^{17}$  (1, 2),  $10^{15}$  (3, 4, 7, 8).

level in the base of the investigated structure. In addition, this figure shows the positions of the levels associated with interstitial iron and the FeB pair. It is worth noting that  $Fe_i$  acts as a deep center; the donor state of the  $Fe_iB_s$  pair shows only negligible recombination activity, while the presence of the acceptor state  $Fe_iB_s$  causes the carrier lifetime to be doping-dependent under low injection conditions [39].

The relationship between  $N_B$  and  $E_F$  is the key factor in the influence of doping level on the sensitivity of photovoltaic parameters to iron presence. Specifically, the rate of SRH recombination — and consequently, variations in photovoltaic parameters due to iron impurities — depends on the relative positioning of  $E_F$  concerning the  $Fe_iB_s$  and  $Fe_i$  levels. Additionally, the equilibrium ratio of  $Fe_iB_s$  and  $Fe_i$  concentrations is also determined by the Fermi level position [60, 61]. Therefore,  $N_B$  affects the number of defects that change their state due to the complete dissociation of  $Fe_iB_s$  pairs, leading to corresponding relative changes in photovoltaic parameters analyzed in this study. Besides, the  $N_B$  concentration also affects the SCR depth (see Fig. 4). The ratio of different charge states for both interstitial iron atoms and iron-boron pairs differs between the SCR and the bulk of the base, leading to distinct SRH recombination rates and variations in photovoltaic conversion efficiency for structures with different doping levels. Furthermore, according to Klaassen's model [58], the concentration of ionized impurities influences charge carrier mobility and, consequently, the diffusion coefficient  $D_n$ , diffusion length  $L_n$ , and photoelectric conversion efficiency (see Eq. (4)). However, the effect of  $N_B$  via  $D_n$  and  $L_n$  is significantly weaker than its influence through  $E_F$  and SCR depth variations. Minor effects are expected as well due to both bandgap narrowing and changes in light absorption by free carriers with varying doping levels. The impact of doping level on photovoltaic parameters has been studied in heterojunction [8], thin-film [10], and perovskite [6] solar cells. Moreover, it has been shown [10] that doping concentration variations affect other barrier structure parameters, such as saturation current and ideality factor.

In our opinion, the change in sign and the monotonic decrease of  $\epsilon I_{SC}$  with increase in doping level value reflect the change in recombination activity caused by the Fermi level shift. It should be noted that at low boron concentrations,  $E_F$  in all points of the base is located below the donor level of  $Fe_i$ , while at  $N_B > 10^{16} \text{ cm}^{-3}$ , they intersect in the vicinity of the  $p$ - $n$  junction — see Fig. 4. The weak dependence on base thickness indicates that the second term in parentheses in Eq. (4) is significantly smaller than the first. In addition, when comparing monochromatic and solar illumination, the latter generates a significantly larger number of non-equilibrium carriers in the emitter due to shorter-wavelength photons. As a result, the emitter current under AM1.5 illumination increases, which, as shown in Eq. (3), leads to a decrease in  $\epsilon I_{SC}$  value.

Fig. 5 illustrates the alterations in the short-circuit current, both observed in experimental studies and calculated for structures with identical base parameters. It should be noted that the figure shows simulation results obtained at various levels of illumination, confirming that  $\epsilon I_{SC}$  is independent of  $W_{\text{ill}}$ .

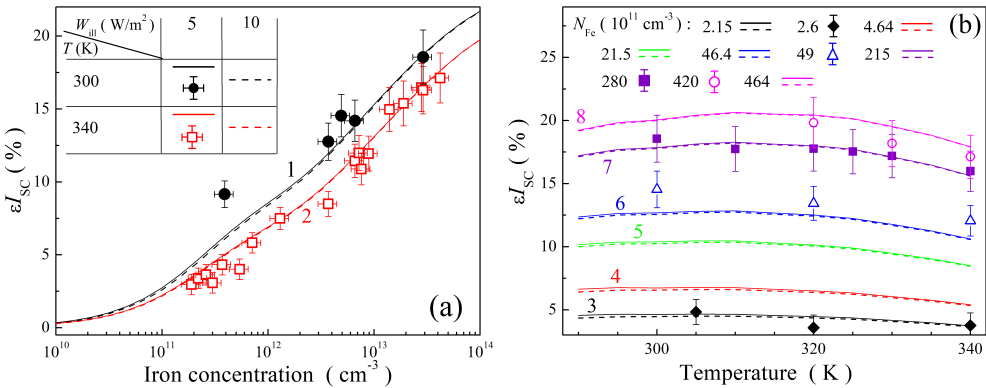


**Figure 5:** Relative changes in short-circuit current caused by a complete dissociation of  $Fe_iB_s$  pairs as a function of iron concentration (a) and temperature (b) for SSC with  $d_p = 380 \mu m$  and  $N_B = 1.36 \times 10^{15} cm^{-3}$  in the case of monochromatic (940 nm) illumination. The marks are the experimental results (divided by factor  $C_{cor} = 1.4$ ), the lines are the simulation results.  $W_{\text{ill}}$ ,  $W/m^2$ : 5 (marks and solid lines), 10 (dotted lines).  $T$ , K (panel a): 300 (1, circles), 340 (2, squares).  $N_{Fe}$ ,  $10^{11} cm^{-3}$  (panel b): 2.15 (curves 3), 2.6 (diamond marks), 4.64 (4), 21.5 (5), 46.4 (6), 49 (triangles), 215 (7), 280 (squares), 420 (circles), 464 (8).

One can see that the theoretical dependencies of  $\varepsilon I_{SC}$  on iron concentration and temperature qualitatively agree with the experimental results. To achieve quantitative agreement, a correction factor of  $C_{cor} = 1.4$  must be applied: the experimentally obtained value  $\varepsilon I_{SC,\text{exp}}$  should be replaced by  $\varepsilon I_{SC,\text{exp}}/C_{cor}$  — as illustrated in Fig. 5. This methodology is frequently cited in the literature [26] and is associated with correcting specific systematic errors in simulations.

As mentioned above, one of the primary objectives of this study is to assess the feasibility of utilizing changes in photoelectric parameters resulting from the dissociation of FeB pairs to estimate iron concentration. One of the most promising approaches in this regard is the application of machine learning algorithms. In this context,  $\varepsilon I_{SC}$  is expected to serve as one of the features. It is worth noting that a popular preprocessing technique involves standardizing feature values, where the distribution of each feature is transformed to have a mean of zero and a standard deviation of one. This approach ensures that multiplying the entire array of  $\varepsilon I_{SC}$  values by a constant does not affect the resulting normalized values.

In our case, simulation errors may arise because certain factors present in actual SSCs were not accounted for in the calculations, specifically:

- the possible influence of series and shunt resistances;
- the antireflective  $SiO_2$  and passivating  $Si_3N_4$  layers on the front surface induce a spectral dependence in reflectance, corresponding calculations necessitating the consideration of multiple reflections [78];
- the shading caused by electrodes;
- the presence of defects unrelated to iron.

Overall, the results indicate that relative changes in short-circuit current following the complete dissociation of FeB pairs can be used to estimate iron concentration:  $\varepsilon I_{SC}$  depends monotonically on  $N_{Fe}$ , and its values can be pretty significant. In this context, determining the amount of impurity atoms is more appropriately conducted using photovoltaic parameters obtained under monochromatic illumination, as this method offers greater sensitivity (response amplitude of  $\varepsilon I_{SC}$ ). However, it should be noted that for low iron concentrations ( $N_{Fe} < 10^{11} cm^{-3}$ ) and solar cells with boron concentrations in the base around  $10^{16} cm^{-3}$ , this approach appears to be unproductive. At these levels, there are blind spots in determining impurity metal concentrations.

### 3.2. Open-circuit voltage

Figure 7 presents the characteristic simulation results of open-circuit voltage changes due to the dissociation of FeB pairs. Figures S7–S12 in the Supplementary Material show additional  $\varepsilon V_{OC}$  dependencies. Notably, the changes in  $V_{OC}$  value are almost an order of magnitude smaller than the values observed for  $I_{SC}$ . Moreover, differences in the behavior of open-circuit voltage changes as a function of iron concentration at low ( $N_B < 2 \times 10^{16} cm^{-3}$ ) base doping levels in the cases of monochromatic and AM1.5 illumination are noteworthy. Under solar illumination,  $\varepsilon V_{OC}$

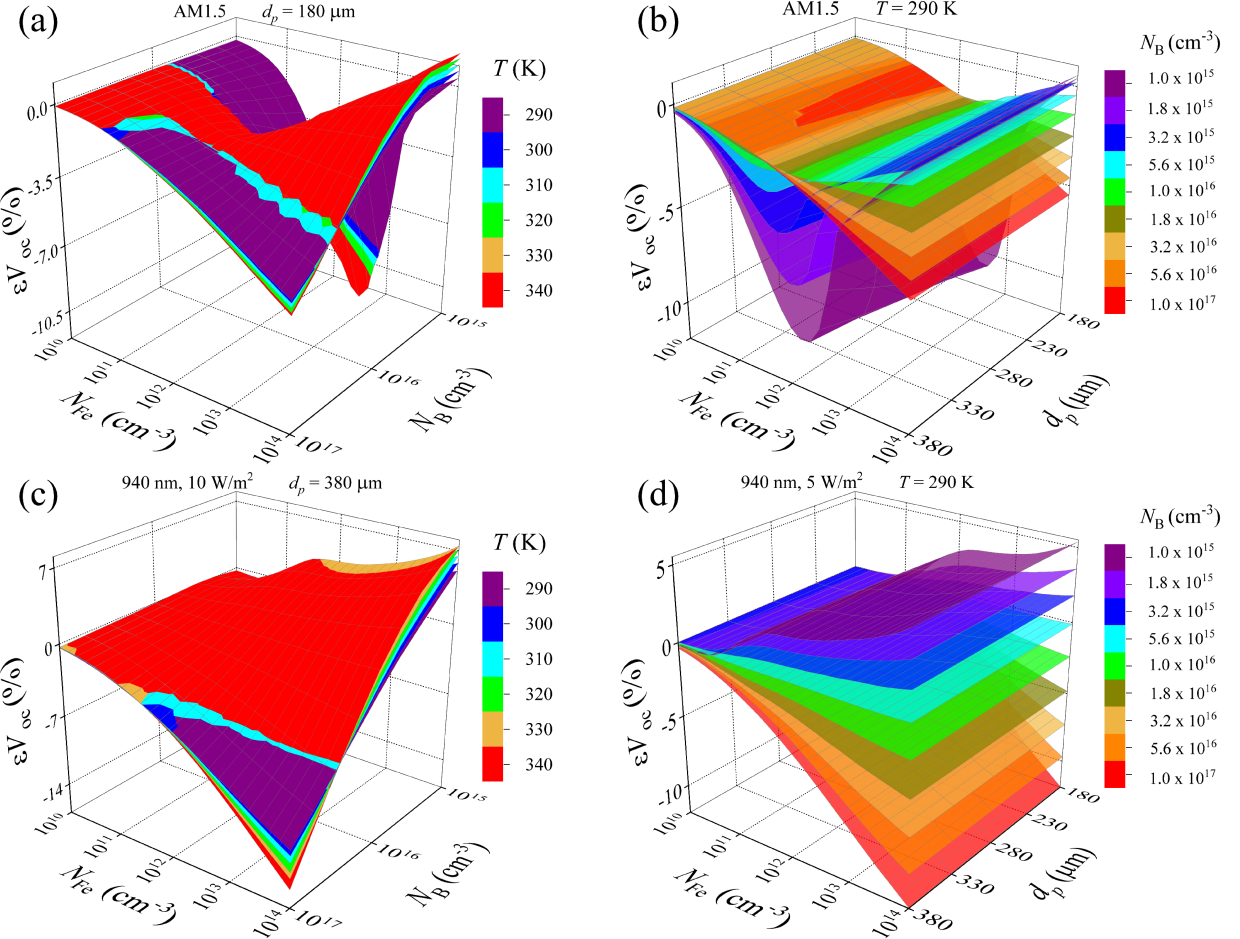


**Figure 6:** Relative changes in open-circuit voltage caused by a complete dissociation of  $\text{Fe}_i\text{B}_s$  pairs as a function of iron concentration and doping level (panels a and c) or base depth (b, d). Illumination: AM1.5 (a, b), 940 nm  $10 \text{ W/m}^2$  (c), 940 nm  $5 \text{ W/m}^2$  (d).  $T, \text{K}$ : 290 (b, d). Different surfaces correspond to different temperatures (a, c) and doping levels (b, d).

values are negative, and the  $\epsilon V_{\text{OC}}$  ( $N_{\text{Fe}}$ ) dependency is non-monotonic — see figs. 6a, 6b. Additionally, the base thickness significantly impacts the iron concentration, which correlates with the minimum  $\epsilon V_{\text{OC}}$  value (Fig. 6a). When illuminated by photons with a wavelength of 940 nm,  $\epsilon V_{\text{OC}}$  values are positive and increase monotonically with iron concentration. As boron concentration increases, the behavior of  $\epsilon V_{\text{OC}}$  ( $N_{\text{Fe}}$ ) becomes similar, regardless of the type of illumination: the relative changes in open-circuit voltage during the rebuilding of iron-containing defects are negative and increase monotonically in absolute value with increasing both  $N_{\text{Fe}}$  and  $N_{\text{B}}$ . Furthermore, changes in  $V_{\text{OC}}$  are more significant under monochromatic illumination, similar to the case of the short-circuit current.

The effect of temperature on  $\epsilon V_{\text{OC}}$  also depends on the base doping level: as  $N_{\text{B}}$  increases, the temperature coefficient of  $\epsilon V_{\text{OC}}$  gradually shifts from positive to negative. This trend is observed for both AM1.5 and 940nm illumination, as shown in Figs. S9, 6a, and 6b. The impact of  $d_p$  on changes in open-circuit voltage is more significant than the effect observed for  $\epsilon I_{\text{SC}}$ . However, base thickness is not a determining factor for  $\epsilon V_{\text{OC}}$ ; it mainly affects low doping levels and temperatures, as shown in Figs. S9, S11, and S12. Another difference between the behavior of  $\epsilon V_{\text{OC}}$  and  $\epsilon I_{\text{SC}}$  is the former dependence on monochromatic illumination intensity. At  $W_{\text{ill}} = 10 \text{ W/m}^2$ , changes in open-circuit voltage are less significant, with differences increasing as iron concentration decreases and showing weak temperature dependence.

Understanding the features of  $\epsilon V_{\text{OC}}$  requires recalling that the open-circuit voltage depends not only on the photocurrent but also on the saturation current  $I_0$  and the ideality factor, which in turn are determined by the state

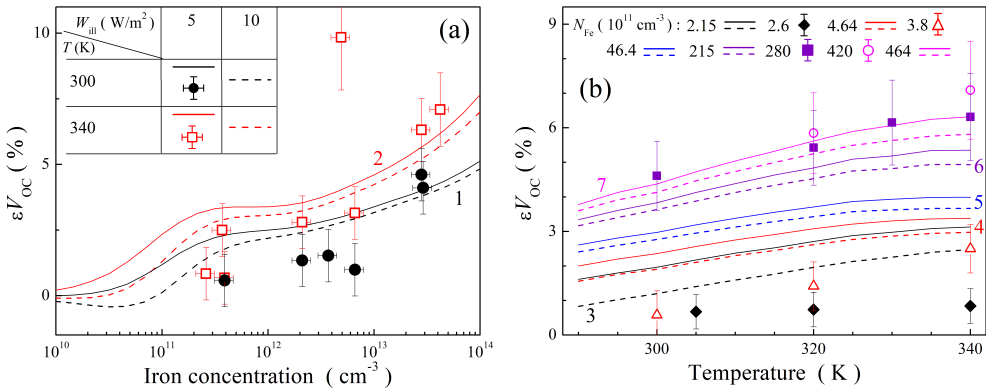


**Figure 7:** Relative changes in open-circuit voltage caused by a complete dissociation of  $\text{Fe}_i\text{B}_s$  pairs as a function of iron concentration (a) and temperature (b) for SSC with  $d_p = 380 \mu\text{m}$  and  $N_B = 1.36 \times 10^{15} \text{ cm}^{-3}$  in the case of monochromatic (940 nm) illumination. The marks are the experimental results, the lines are the simulation results.  $W_{\text{int}}$ ,  $\text{W/m}^2$ : 5 (marks and solid lines), 10 (dotted lines).  $T$ ,  $\text{K}$  (panel a): 300 (1, circles), 340 (2, squares).  $N_{\text{Fe}}$ ,  $10^{11} \text{ cm}^{-3}$  (panel b): 2.15 (curves 3), 2.6 (diamond marks), 4.64 (4), 3.8 (triangles), 46.4 (5), 215 (6), 280 (squares), 420 (circles), 464 (7).

of the defect subsystem and other parameters that varied in simulation [37, 75]. In the case of simplified single-diode model [75]:

$$V_{\text{OC}} = nkT \left[ \ln \left( \frac{I_{\text{ph}}}{I_0} \right) + 1 \right]. \quad (5)$$

Similar to the photocurrent, we can express  $I_0$  as the sum of the currents from the base and the emitter [76]:

$$I_0 = I_{0,\text{e}} + I_{0,\text{b}}, \quad (6)$$

and the second term can be expressed as follows [77]:

$$I_{0,\text{b}} = \frac{qn_i D_n}{N_B L_n} \cdot \frac{\frac{D_n}{SL_n} \sinh \left( \frac{d_p}{L_n} \right) + \cosh \left( \frac{d_p}{L_n} \right)}{\sinh \left( \frac{d_p}{L_n} \right) + \frac{D_n}{SL_n} \cosh \left( \frac{d_p}{L_n} \right)}, \quad (7)$$

where  $n_i$  is the intrinsic carrier concentration. The last equation explains the observed dependence of  $\varepsilon V_{\text{OC}}$  on the base thickness.

It was shown [38, 37] previously that changes in the ideality factor during restructuring  $\text{Fe}_i\text{B}_{\text{Si}} \rightleftharpoons \text{Fe}_i + \text{B}_{\text{Si}}$  do not exceed a few percent. This  $n$  slight variation, combined with the logarithmic dependence of  $V_{\text{OC}}$  on  $I_{\text{ph}}$  as shown in Eq. (5), explains the small absolute values of  $\varepsilon V_{\text{OC}}$ .

Schmidt [39] attributes the non-monotonic dependence of  $\varepsilon V_{\text{OC}}$  ( $N_{\text{Fe}}$ ) (Fig. 6b) to the significantly higher injection level in the cell base under open-circuit conditions compared to short-circuit conditions. Overall, the results support this hypothesis. In fact, for monochromatic illumination with significantly lower intensity, the injection level remains below the crossover point [39] throughout the  $I$ - $V$  curve, which results in the absence of a minimum in the  $\varepsilon V_{\text{OC}}$  ( $N_{\text{Fe}}$ ) dependence.

The data presented in Fig. 7 compare the experimental and simulation results. Overall, the results in both cases are qualitatively consistent. However, to ensure that the absolute values are consistent, a correction factor dependent on iron concentration must be used. According to the data,  $C_{\text{cor}}$  is less than 1 for low values of  $N_{\text{Fe}}$  and greater than 1 for high values. By the way, Schubert et al. [26] also observed such dependence of the correction factor.

It is believed [75] that the main effect of metals on the  $V_{\text{OC}}$  values can be determined by shunt formation. However, SCAPS does not account for the effect of shunt resistance, which we believe is the primary reason for the discrepancies between experimental and simulated values.

In summary, using relative changes in open-circuit voltage due to FeB pair dissociation is less convenient for estimating iron concentration compared to  $\varepsilon I_{\text{SC}}$ . It is because of the smaller absolute values of  $\varepsilon V_{\text{OC}}$ , the non-monotonic dependence of  $\varepsilon V_{\text{OC}}$  on  $N_{\text{Fe}}$  under certain conditions, and the need for precise control over the intensity

of monochromatic illumination. However, using  $\epsilon V_{OC}$  as an additional parameter alongside  $\epsilon I_{SC}$  can significantly enhance the accuracy of iron concentration measurements for  $N_{Fe} < 10^{11} \text{ cm}^{-3}$  and  $N_B = (1 - 5) \times 10^{15} \text{ cm}^{-3}$  under AM1.5 illumination. In this case, the dependence of  $\epsilon V_{OC}$  on  $N_{Fe}$  is sufficiently sharp (Fig. 6b), and ambiguity in associating specific  $\epsilon V_{OC}$  values with iron concentration can be resolved by the monotonic behavior of  $\epsilon V_{OC}$  in this range. Notably, these boron concentrations are most relevant to typical real SSCs.

### 3.3. Fill factor

The fill factor is another defining term in the overall behavior of a solar cell.  $FF$  is the ratio of the maximum obtainable power to the product of short circuit current and open-circuit voltage. In general,  $FF$  depends on both  $I_{SC}$  and  $V_{OC}$ . However, it can be shown that it is mainly determined by the  $V_{OC}$  value. Indeed, it is shown [75] within the single-diode model

$$FF \approx \frac{v_{OC} - \ln(1 + v_{OC})}{v_{OC} + 1}, \quad (8)$$

with  $v_{OC}$  being the normalized open-circuit voltage  $v_{OC} = qV_{OC}/nkT$ . Another well-known empirical relation for the maximum achievable fill factor of a solar cell is proposed by Green [79, 80]:

$$FF \approx \frac{v_{OC} - \ln(0.72 + v_{OC})}{v_{OC} + 1}. \quad (9)$$

Thus, any factors that affect  $V_{OC}$  also impact the  $FF$ . However, since  $V_{OC}$  appears in both the numerator and denominator of Eqs. (8)-(9), the resulting changes in the fill factor are expected to be smaller than those in the open-circuit voltage.

Recently, Bothe et al. [81] proposed explicit expressions for the  $FF$  in terms of other key solar cell parameters. Specifically, for  $p$ -type SSCs and intrinsic limits, the parameterization can be expressed as follows:

$$FF = \frac{90.4924}{d_p^{0.00220}} \left[ 0.9478 + \frac{0.0519}{1 + \left( \frac{\log N_B}{17.3739 d_p^{-0.0093}} \right)^{76.3}} \right], \quad (10)$$

where  $d_p$  is expected to be in micrometers. Additional recombination (e.g., Shockley–Read–Hall) leads to a decrease in  $FF$  value [81].

Figs. S13–S16 in the Supplementary Material, along with Fig. 8, illustrate how the fill factor varies with iron defect variability. The following features of  $\epsilon FF$  can be identified from the presented data:

- The changes in the fill factor are the smallest among the parameters considered, with maximum  $\epsilon FF$  values not exceeding 10%;
- At low boron concentrations ( $N_B < 10^{16} \text{ cm}^{-3}$ ), the dependence of  $\epsilon FF$  on  $N_{Fe}$  is notably non-linear. Within the used concentration range, two regions of decrease and two regions of increase in  $\epsilon FF$  are observed. A similar relationship between the fill factor and defect concentration was observed in BaZrSe<sub>3</sub>–based perovskite solar cells [6];
- At low boron concentrations, the change in fill factor value is positive and, in contrast to  $\epsilon V_{OC}$  and  $\epsilon I_{SC}$ , AM1.5 illumination causes more significant changes in  $\epsilon FF$  than monochromatic illumination. At high boron concentrations, the  $\epsilon FF$  is negative and does not exceed 4%;
- The absolute value of  $\epsilon FF$  increases, regardless of the value sign, with temperature increases;
- Increasing the base thickness leads to a decrease in  $\epsilon FF$  (a reduction in the fill factor with increasing  $d_p$  is expected according to (10)). Additionally, this results in a shift of the  $\epsilon FF$  ( $N_{Fe}$ ) dependence towards lower iron concentrations. The impact of  $d_p$  is more pronounced at low boron concentrations and in the case of AM1.5 illumination;
- In the case of monochromatic illumination, the light intensity significantly affects the relative changes in the fill factor ( $\epsilon FF$  can vary by a factor of 2 when  $W_{ill}$  changes from 5 to 10 W/m<sup>2</sup>). This impact is influenced by both iron concentration (which can even change the sign of the effect) and temperature.

Fig. 9 shows that the experimental dependencies of  $\epsilon FF$  ( $N_{Fe}$ ) and  $\epsilon FF$  ( $T$ ) align well with the calculated values.

Figure 9 shows that the experimental dependencies  $\epsilon FF$  ( $N_{Fe}$ ) and  $\epsilon FF$  ( $T$ ) are in good agreement with the calculated values. In our opinion, the quantitative agreement is limited by the relatively low accuracy of  $\epsilon FF$

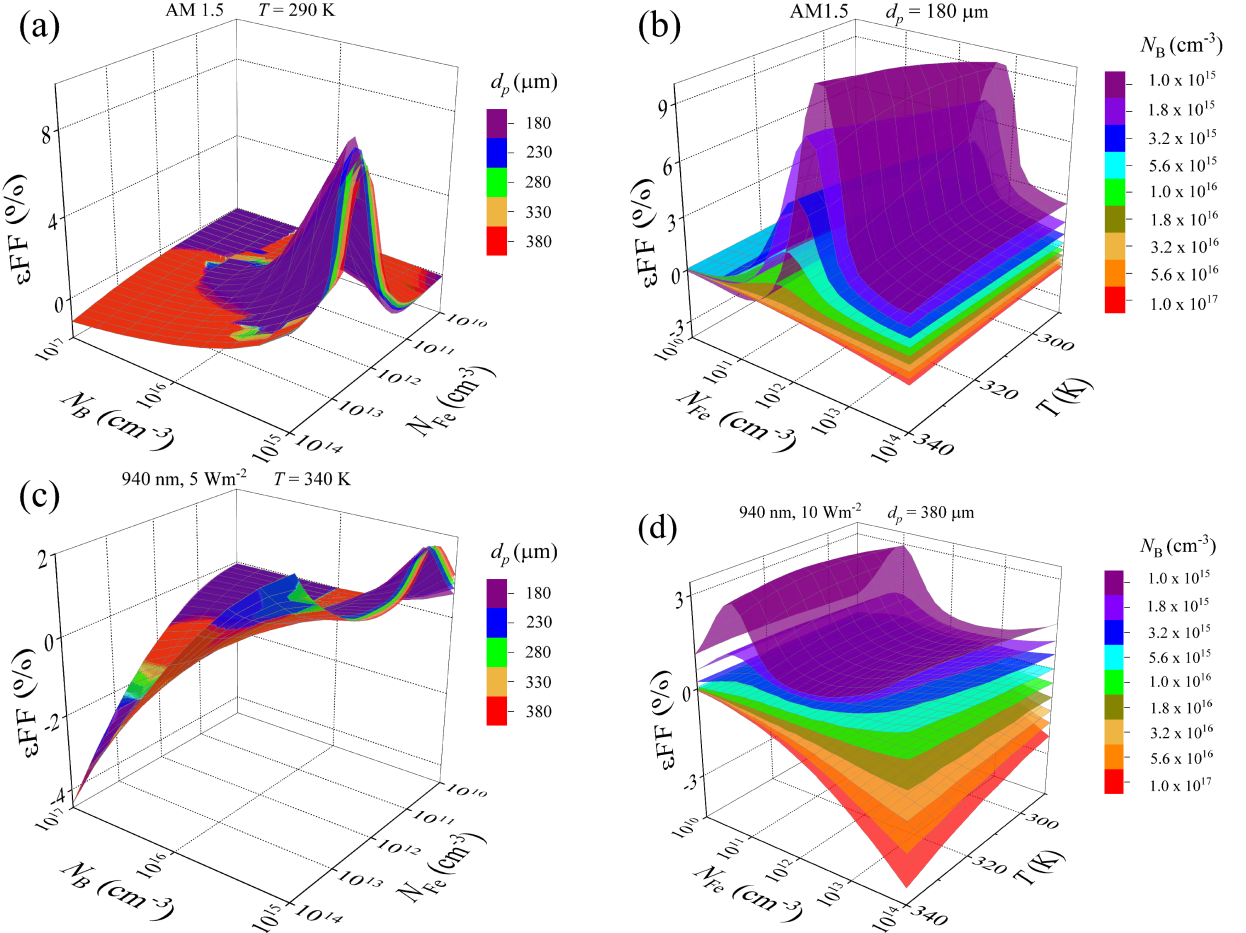


**Figure 8:** Relative changes in fill factor caused by a complete dissociation of  $\text{Fe}_x\text{B}_y$  pairs as a function of iron concentration and doping level (panels a and c) or temperature (b, d). Illumination: AM1.5 (a, b), 940 nm 5  $\text{W}/\text{m}^2$  (c), 940 nm 10  $\text{W}/\text{m}^2$  (d).  $T$ , K: 290 (a), 340 (c).  $d_p$ ,  $\mu\text{m}$ : 180 (b), 380 (d). Different surfaces correspond to different base depths (a, c) and doping levels (b, d).

measurements and the dependence of fill factor on series and shunt resistances [79, 80], which were not considered in the simulation.

The observed characteristics of  $\epsilon FF$  suggest that the fill factor is considerably less suitable for estimating iron concentration in SSCs than the short-circuit current and open-circuit voltage.  $\epsilon FF$  can serve as an auxiliary parameter to refine  $N_{\text{Fe}}$ ; however, if monochromatic illumination is used, light intensity must be controlled with high precision.

### 3.4. Solar cell efficiency

Solar cell efficiency depends on all the photovoltaic conversion parameters previously discussed:

$$\eta = \frac{I_{\text{SC}} V_{\text{OC}} \text{FF}}{W_{\text{ill}} A}, \quad (11)$$

where  $A$  is the illuminated area of the solar cell. Considering the differential of Eq. (11), a cumulative effect on the relative changes in efficiency can be anticipated.

Considering the differential of formula (11):

$$d\eta = \frac{dI_{\text{SC}}}{I_{\text{SC}}} + \frac{dV_{\text{OC}}}{V_{\text{OC}}} + \frac{d\text{FF}}{\text{FF}}, \quad (12)$$

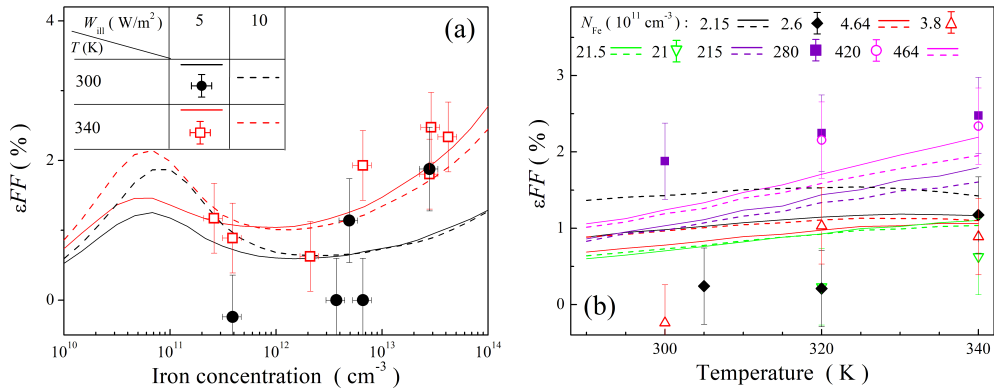


**Figure 9:** Relative changes in fill factor caused by a complete dissociation of  $\text{Fe}_i\text{B}_s$  pairs as a function of iron concentration (a) and temperature (b) for SSC with  $d_p = 380 \mu\text{m}$  and  $N_B = 1.36 \times 10^{15} \text{ cm}^{-3}$  in the case of monochromatic (940 nm) illumination. The marks are the experimental results, the lines are the simulation results.  $W_{\text{ill}}$ , W/m<sup>2</sup>: 5 (marks and solid lines), 10 (dotted lines). Different lines and marks correspond to different temperatures (a) or  $N_{Fe}$  values (b) — see legends.

a cumulative effect on the relative changes in efficiency can be anticipated. Fig. 10 illustrates the simulation results for the solar cell efficiency, while Figs. S17–S20 offer additional details in the Supplementary Material.

The data indicate that the primary features of the  $\epsilon\eta$  dependencies on solar cell parameters and temperature align with those observed for  $\epsilon I_{SC}$ . However, a few differences are evident: 1) the amplitude of  $\epsilon\eta$  is enhanced, reaching up to 50% for AM1.5 and 200% for 940 nm; these results align with the expectations from Eq. (12) and make SC efficiency more convenient for iron concentration estimating; 2) for AM1.5, in the region  $N_B < 5 \times 10^{15} \text{ cm}^{-3}$ , a non-monotonic dependence of  $\epsilon\eta(N_{Fe})$  is observed, rendering it impossible to use relative changes in efficiency as the sole parameter for iron concentration estimating under specified conditions; 3) the existing dependence of  $\epsilon\eta$  on the intensity of the monochromatic illumination is weak, which does not prevent the use of  $\epsilon\eta$  for determining  $N_{Fe}$ , even with not very precise  $W_{\text{ill}}$  measurements; 4) the temperature dependence of  $\epsilon\eta$  is weaker than that of  $\epsilon I_{SC}$ .

Fig. 11 shows the experimental and simulated values of changes in the efficiency of the solar cell with a  $380 \mu\text{m}$  base thickness and a doping concentration of  $1.36 \times 10^{15} \text{ cm}^{-3}$ . When presenting the experimental data, the same correction factor,  $C_{\text{cor}} = 1.4$ , was applied as in the case of the short-circuit current. The data align closely, indicating that the inaccuracies typical for  $V_{OC}$  and  $FF$  do not significantly contribute.

The revealed characteristics of  $\epsilon\eta$  indicate that this photoelectric parameter is entirely suitable for estimating iron concentration.

Two key metrics were used to identify the solar cell parameter whose changes, resulting from the  $\text{Fe}_i\text{B}_{Si} \rightleftharpoons \text{Fe}_i + \text{B}_{Si}$  reconstruction, enable the most reliable determination of iron concentration. Specifically, these metrics are: (1) the monotonicity of the relative change in the parameter value as a function of impurity concentration, which is a necessary condition for the unambiguous estimation of  $N_{Fe}$ ; and (2) the absolute magnitude of the parameter change, which allows for more precise measurements and, consequently, a more accurate estimation of  $N_{Fe}$ . The first criterion is not satisfied by  $\epsilon_{FF}$ ,  $\epsilon V_{OC}$ , and  $\epsilon\eta$  (the latter two under AM1.5 illumination). At the same iron concentration,  $\epsilon I_{SC}$  values under monochromatic illumination exceed those under AM1.5 illumination. As mentioned earlier, this effect deals with differences in the generation locations of non-equilibrium carriers under different lighting conditions. Additionally, under identical conditions, the changes in open-circuit voltage are significantly weaker than those in short-circuit current or efficiency. Since  $\epsilon I_{SC}$  and  $\epsilon\eta$  are of the same order, it is advisable to select the more reliable parameter using additional metrics. Notably, short-circuit current determination, unlike efficiency, does not require additional calculations and can be directly extracted from the raw measured  $I$ - $V$  curves. Furthermore,  $\epsilon I_{SC}$  is virtually independent of illumination intensity (whereas  $\epsilon\eta$  exhibits a weak dependence), leading to two key advantages: (a) iron concentration can be determined using an uncalibrated for-intensity monochromatic light source; (b) the influence of shading caused by electrodes, along with the antireflective and passivating layers of the solar cell, is reduced.

### 3.5. Photoelectric parameters correlation

The previous subsections demonstrated that by using the relative changes in photovoltaic energy conversion parameters following the dissociation of FeB pairs (e.g., changes in short-circuit current), along with considering

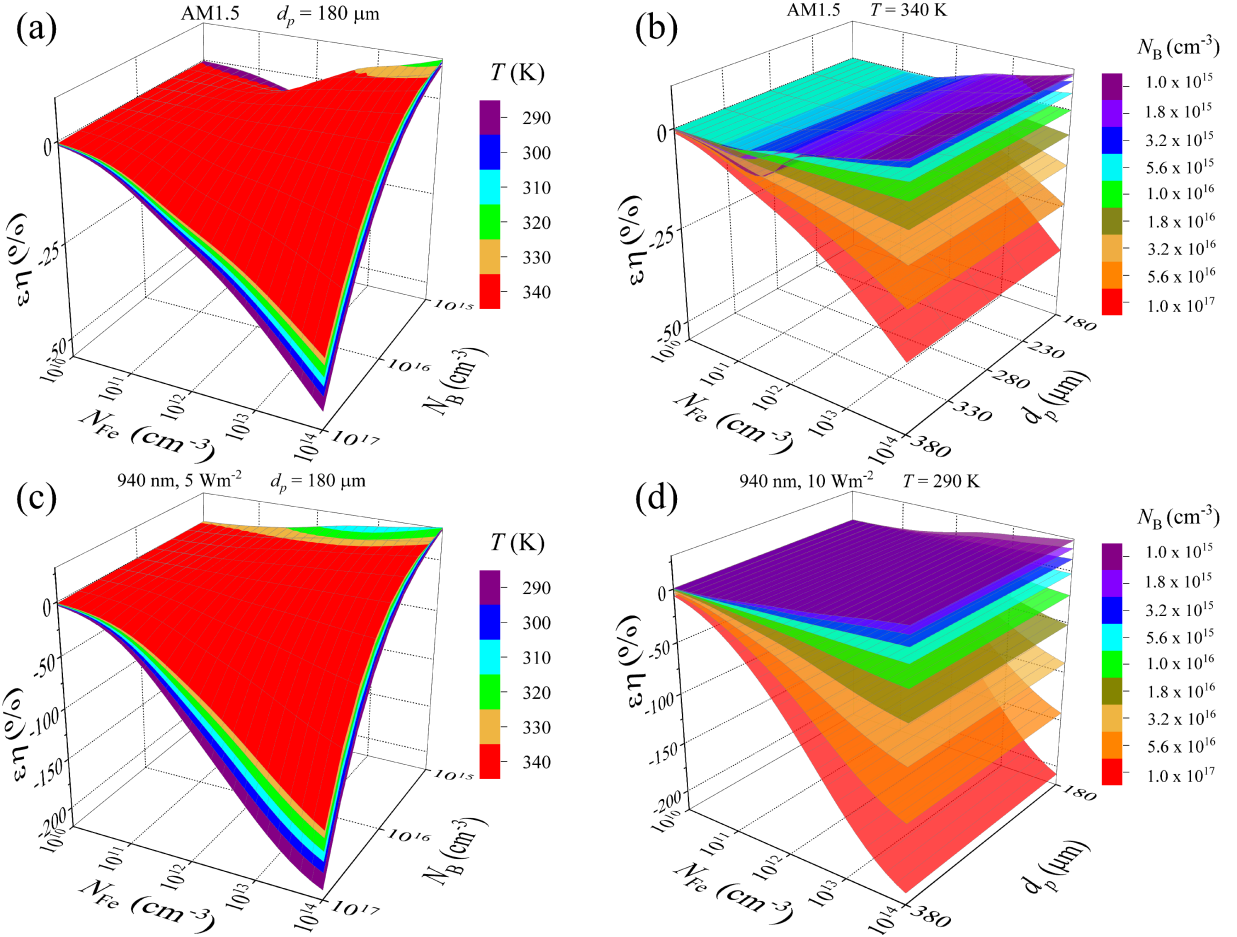


**Figure 10:** Relative changes in SSC efficiency caused by a complete dissociation of  $\text{Fe}_i\text{B}_s$  pairs as a function of iron concentration and doping level (panels a and c) or base depth (b, d). Illumination: AM1.5 (a, b), 940 nm  $5 \text{ W/m}^2$  (c), 940 nm  $10 \text{ W/m}^2$  (d).  $T, \text{K}$ : 290 (d), 340 (b).  $d_p, \mu\text{m}$ : 180 (a, c). Different surfaces correspond to different temperatures (a, c) and doping levels (b, d).

solar cell parameters (such as base depth and doping level) and measurement conditions (such as temperature and illumination type), it is possible to predict iron concentration. One approach to evaluating the value of  $N_{\text{Fe}}$  is to apply a machine learning algorithm (random forest, gradient booster, or artificial neural network etc.). If we assume that the training process is conducted separately for each illumination variant and want to determine the magnitude of  $N_{\text{Fe}}$  based on changes in short-circuit current, the input set of descriptors could be  $(T, d_p, N_B, \epsilon I_{\text{SC}})$ . Evidently, incorporating additional information, such as changes in efficiency ( $\epsilon\eta$ ), along with an expanded set of descriptors  $(T, d_p, N_B, \epsilon I_{\text{SC}}, \epsilon\eta)$ , increases the complexity of calculations due to the growing number of input parameters. However, this should enhance the accuracy of  $N_{\text{Fe}}$  predictions. At the same time, when comparing Fig. 3 and Fig. 10, it is clear that  $\epsilon I_{\text{SC}}$  and  $\epsilon\eta$  are not entirely independent. This outcome is understandable from a physical standpoint as short-circuit current and efficiency characterize the same physical process — the diffusion of photo-induced carriers. Thus, the set  $(T, d_p, N_B, \epsilon I_{\text{SC}}, \epsilon\eta)$  contains useful and redundant information compared to  $(T, d_p, N_B, \epsilon I_{\text{SC}})$ .

Analyzing their correlations can help evaluate the independence of the parameters. Fig. 12 presents the Pearson correlation coefficients calculated for all parameter sets. Additionally, it shows the correlation between iron concentration and each input parameter. It's worth noting that the  $N_{\text{Fe}}$  and  $N_B$  values in the logarithmic scale were used in calculations. It is a common approach for quantities that span several orders of magnitude [82].

Firstly, it is noteworthy that, as indicated by the obtained data, the value of  $N_{\text{Fe}}$  exhibits a weak correlation with each descriptor. Consequently, using any parameter in isolation from others is not feasible for precise iron

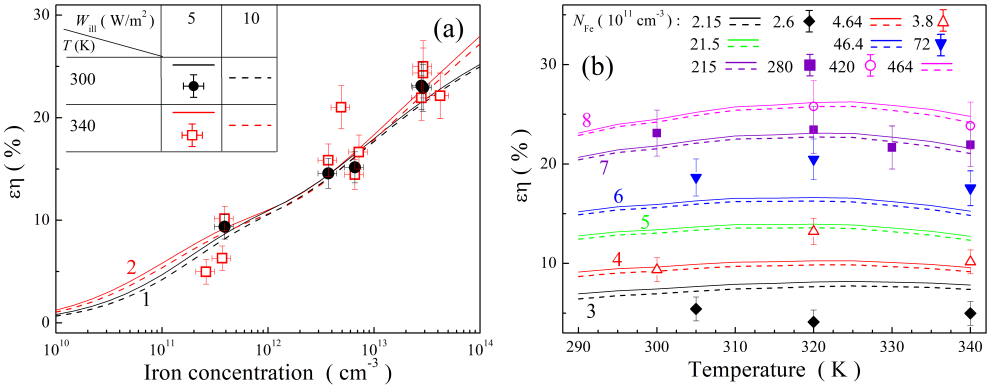


**Figure 11:** Relative changes in SSC efficiency caused by a complete dissociation of  $\text{Fe}_i\text{B}_s$  pairs as a function of iron concentration (a) and temperature (b) for SSC with  $d_p = 380 \mu\text{m}$  and  $N_B = 1.36 \times 10^{15} \text{ cm}^{-3}$  in the case of monochromatic (940 nm) illumination. The marks are the experimental results (divided by factor  $C_{\text{cor}} = 1.4$ ), the lines are the simulation results.  $W_{\text{ill}}$ ,  $\text{W/m}^2$ : 5 (marks and solid lines), 10 (dotted lines).  $T$ , K (panel a): 300 (1, circles), 340 (2, squares).  $N_{\text{Fe}}$ ,  $10^{11} \text{ cm}^{-3}$  (panel b): 2.15 (curves 3), 2.6 (diamond marks), 3.8 (open triangles), 4.64 (4), 21.5 (5), 46.4 (6), 72 (filled triangles), 215 (7), 280 (squares), 420 (circles), 464 (8).

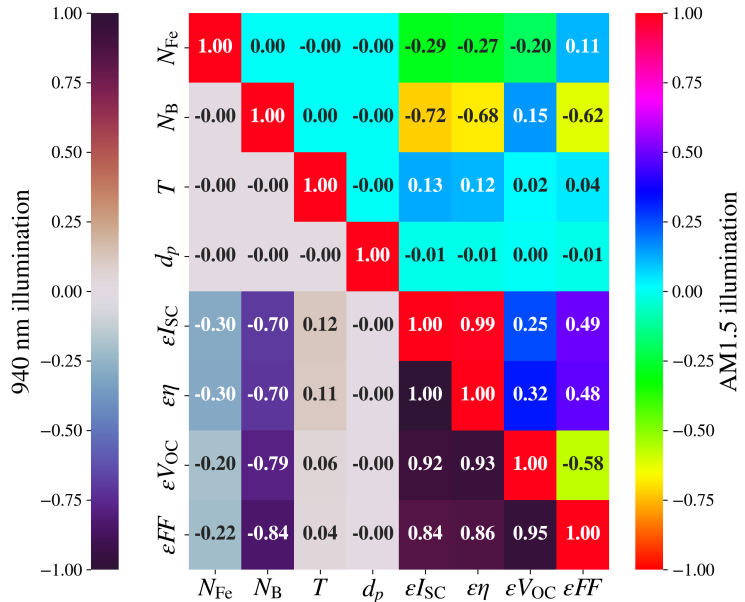


**Figure 12:** Correlation plot of photoelectric conversion parameters and solar cell characteristics. Data above and below the main diagonal correspond to AM1.5 and 940 nm (5  $\text{W/m}^2$ ) illumination, respectively.

concentration estimation. Regarding the descriptors associated with photovoltaic energy conversion, all of these parameters correlate strongly with the base doping level, except for open-circuit voltage under AM1.5 illumination. In addition, these parameters are substantially correlated with each other, which is particularly noticeable when using monochromatic illumination. Thus, augmenting the descriptor set by incorporating relative changes in additional photoelectric parameters introduces substantial redundancy in the input data.

To assess the degree of redundancy information in different descriptor sets, we employed Principal Component Analysis (PCA), widely used in solving various problems, including identifying defects in solar cells [83]. PCA uses a linear combination of the original variables to construct the new variables (principal component, PC) while keeping maximum variance information. PCs are uncorrelated, and PCA allows one to evaluate each PC's contribution to the

**Table 2**

PSA results for sets of variables that serve to estimate the iron concentration in SSC. The numbers represent the ratio of information variance associated with each principal component when using AM1.5 illumination / 940 nm illumination.

set of descriptors	Explained Variance Ratio (%)						
	PC0	PC1	PC2	PC3	PC4	PC5	PC6
( $T, d_p, N_B, \epsilon I_{SC}$ )	43.23/42.80	25.00/25.00	25.00/25.00	6.70/7.20	—	—	—
( $T, d_p, N_B, \epsilon I_{SC}, \epsilon\eta$ )	52.39/52.46	20.00/20.00	20.00/20.00	7.48/7.51	0.13/0.03	—	—
( $T, d_p, N_B, \epsilon I_{SC}, \epsilon\eta, \epsilon V_{OC}$ )	44.40/59.02	18.78/16.73	16.67/16.67	16.46/6.28	3.61/1.29	0.08/0.01	—
( $T, d_p, N_B, \epsilon I_{SC}, \epsilon\eta, \epsilon V_{OC}, \epsilon FF$ )	43.29/63.24	22.59/14.41	14.29/14.29	14.19/5.65	4.29/1.95	1.35/0.46	0.002/0.01

total variance of the information. In the case of some particular principal component having a low information variance ratio, it can be discarded with little to no loss of useful information.

PCs were built for different combinations of photovoltaic parameters and solar cell characteristics for the full set of simulated data, and the results are listed in Table 2. As evident, when only changes in short-circuit current are considered along with the solar cell's base parameters and temperature, no excessive information is present (in the case of the descriptor set ( $T, d_p, N_B, \epsilon I_{SC}$ ), all four principal components exhibit a high ratio of information variance). And vice versa, when estimating  $N_{Fe}$  using a maximal set of seven descriptors ( $T, d_p, N_B, \epsilon I_{SC}, \epsilon\eta, \epsilon V_{OC}, \epsilon FF$ ) obtained under monochromatic illumination five PCs account for more than 99.5% of the variance in the input data. Therefore, applying PCA to transform the seven input variables and using only five is fully justified, as it significantly simplifies calculations with minimal impact on estimation accuracy. For the same set of descriptors obtained under AM1.5 illumination, the number of really independent variables is six. In general, if the estimation of iron concentration is based on changes in multiple photovoltaic parameters, it is advisable to apply PCA to transform the original data. Thus, the simultaneous use of  $\epsilon\eta$  and  $\epsilon I_{SC}$  practically does not alter the number of independent variables (four) compared to the initial set of descriptors. With the additional use of  $\epsilon V_{OC}$  values obtained under AM1.5 illumination, it is advisable to consider five independent variables. For the same set of descriptors in a monochromatic illumination case, one can limit oneself to using only four independent components (cumulative variance ratio for PC4 and PC5 does not exceed 1.3%).

#### 4. Conclusion

We have provided the results of modeling the impact of variations in the state of iron impurities on the photovoltaic parameters of silicon solar cells with different base properties under various external conditions (temperature, intensity, and spectral composition of illumination). The simulation results have been compared with experimental data.

The feasibility of using relative changes in short-circuit current, open-circuit voltage, fill factor, and efficiency resulting from the dissociation of FeB pairs to estimate the concentration of iron impurities in a solar cell has been analyzed. It is shown that short-circuit current is the most suitable parameter for iron quantification, as variations in  $I_{SC}$  value during the  $Fe_iB_{Si} \rightleftharpoons Fe_i + B_{Si}$  transformation can be effectively utilized. Determining photovoltaic parameters under monochromatic illumination, with a wavelength corresponding to the predominant absorption in the solar cell base, is more effective than using AM1.5 illumination. The most viable alternatives are solar cell efficiency and open-circuit voltage; however, their applicability is limited at low base doping levels ( $< 10^{16} \text{ cm}^{-3}$ ) due to non-monotonic variations in response to increasing iron concentration. In our view, using the fill factor for iron concentration estimation is impractical. These conclusions are validated by experimental results, which show that short-circuit current provides the most accurate determination of iron concentration.

It has been shown that the potential accuracy of estimating iron concentration depends on the doping level of the base: at a boron concentration around  $10^{16} \text{ cm}^{-3}$ , it is minimal, while decreasing or increasing this value enhances the response of  $I_{SC}$  to the presence of iron. Furthermore, the accuracy of  $N_{Fe}$  determination is significantly influenced by the availability of precise information on the doping level of the base, as well as the accuracy of estimating the intensity of monochromatic illumination, especially when using  $\epsilon\eta$  and  $\epsilon V_{OC}$ .

At the same time,  $\epsilon\eta$  and  $\epsilon V_{OC}$  can serve as additional parameters for refining the determination of iron concentration. In our opinion, for estimating iron concentration through changes in photovoltaic parameters due to variability in iron-related defects, it is advisable to use a set of ( $T, d_p, N_B, \epsilon I_{SC}, \epsilon\eta$ ) or ( $T, d_p, N_B, \epsilon I_{SC}, \epsilon\eta, \epsilon V_{OC}$ ). Furthermore, it has been demonstrated that iron-induced changes in various photovoltaic parameters are correlated.

Therefore, if iron concentration estimation is performed using changes in multiple photovoltaic parameters, applying Principal Component Analysis is advisable. This data transformation reduces the number of variables while preserving the maximum variance information and accelerating calculations.

Our study lays the groundwork for developing an efficient, express, cost-effective method for monitoring iron impurity concentrations in silicon solar cells. This approach relies on current-voltage measurements and can be easily incorporated into the standard characterization procedure for silicon photovoltaic devices. Through simulations and experiments, we have identified a key metric for quantifying iron impurities (short-circuit current) and determined which factors significantly (base doping level, temperature) and insignificantly (base thickness) influence the response of solar cells to iron-related defect rearrangements. These findings should be considered when implementing the method in practice. Our approach allows for the simultaneous determination of the concentration of iron impurities along with the standard solar cell parameters (such as short-circuit current, open-circuit voltage, and nominal power), all without needing additional equipment. The suggested and verified approach advances our understanding of impurity effects and paves the way for improved solar cell reliability.

## Acknowledgments

O.O. would like to acknowledge the financial support by National Research Foundation of Ukraine (Project No. 2023.03/0252 “Development of principles for the creation and machine-oriented characterization of porous silicon nanostructures with optimal heat transport properties”)

## Supplementary data

Supplementary data to this article can be found online at <http://surl.li/qneich>

## Data availability

Data will be made available on request.

## References

- [1] B. P. Singh, S. K. Goyal, S. S. A., Grid connected-photovoltaic system (GC-PVS): Issues and challenges, IOP Conference Series: Materials Science and Engineering 594 (2019) 012032.
- [2] M. J. Paul, R. Suresh, P. Gayathri, V. Balasubramani, K. M. Al-Anazi, M. A. Farah, Cuo-la2o3 composite-enabled mis schottky barrier diodes: A novel approach to optoelectronic device diversification, J. Inorg. Organomet. Polym. Mater. (2024).
- [3] P. Gayathri, T. Akila, G. A. Sibu, M. Selvaraj, M. A. Assiri, P. matheswaran, V. Balasubramani, Enhancing photovoltaic applications through precipitating agents in ito/cis/ceo2/al heterojunction solar cell, Inorg. Chem. Commun. 168 (2024) 112866.
- [4] D. Behera, A. Dixit, A. Azzouz-Rached, A. Bentouaf, M. Ferdous Rahman, H. Albalawi, A. Bouhenna, E. S. Yousef, R. Sharma, Prediction of new max phase zr2msic2 ( $m = ti, v$ ) compounds as a promising candidate for future engineering: DFT calculations, Materials Science and Engineering: B 301 (2024) 117141.
- [5] A. Azzouz-Rached, M. Azzouz-Rached, N. Rahman, M. Husain, N. Sfina, V. Tirth, A. Bentouaf, M. Ferdous Rahman, N. Algethami, H. A. Althobaiti, K. M. Abualnaja, G. Alosaimi, Exploring highly energetic quaternary double transition metal max phase m2scsic2 ( $m = ti, v$ ) composition along with ab-initio assessments, Inorg. Chem. Commun. 167 (2024) 112785.
- [6] M. Masum Mia, M. Faruk Hossain, M. Rahman, N. Badi, A. Irfan, M. Ferdous Rahman, Unveiling the impact of se based htm on bazrse3 perovskites solar cell and improving the theoretical efficiency above 32%, Materials Science and Engineering: B 311 (2025) 117817.
- [7] M. F. Rahman, M. A. B. Shanto, M. A. Ali, L. Marasamy, A. Benami, A. R. Chaudhry, A. Irfan, A new exploration of the impact of different wide-bandgap s-chalcogenides electron transport layers (etl) on the performance of basi2-based solar cells, Emergent Materials (2024).
- [8] B. Sultana, M. Ferdous Rahman, A. Chandra Roy, M. Masum Mia, M. Al Ijajul Islam, A. Irfan, A. Rasool Chaudhry, M. Dulal Haque, A novel design and optimization of si based high performance double absorber heterojunction solar cell, Materials Science and Engineering: B 304 (2024) 117360.
- [9] G. Alan Sibu, P. Gayathri, T. Akila, R. Marnadu, V. Balasubramani, Manifestation on the choice of a suitable combination of mis for proficient schottky diodes for optoelectronic applications: A comprehensive review, Nano Energy 125 (2024) 109534.
- [10] T. Akila, P. Gayathri, G. Alan Sibu, V. Balasubramani, H. Al-Lohedan, D. M. Al-Dhayan, Augmented photovoltaic performance of cu/ce-(sn:cd)/n-si schottky barrier diode utilizing dual-doped ce-(sn:cd) thin films, Opt. Mater. 149 (2024) 115133.
- [11] R. Basnet, D. Yan, D. Kang, M. M. Shehata, P. Phang, T. Truong, J. Bullock, H. Shen, D. Macdonald, Current status and challenges for hole-selective poly-silicon based passivating contacts, Appl. Phys. Rev. 11 (2024) 011311.
- [12] L. Wang, J. Liu, Y. Li, G. Wei, Q. Li, Z. Fan, H. Liu, Y. An, C. Liu, J. Li, Y. Fu, Q. Liu, D. He, Dislocations in crystalline silicon solar cells, Advanced Energy and Sustainability Research 5 (2024) 2300240.
- [13] C. Claeys, E. Simoen, Metal Impurities in Silicon- and Germanium-Based Technologies: Origin, Characterization, Control, and Device Impact, volume 270 of *Springer Series in Materials Science*, Springer International Publishing, Berlin/New York, 2018.

- [14] A. Goetzberger, W. Shockley, Metal Precipitates in Silicon p-n Junctions, *J. Appl. Phys.* 31 (1960) 1821–1824.
- [15] O. Breitenstein, J. P. Rakotonaina, M. H. Al Rifai, M. Werner, Shunt types in crystalline silicon solar cells, *Prog. Photovolt.: Res. Appl.* 12 (2004) 529–538.
- [16] K. Lee, A. Nussbaum, The influences of traps on the generation-recombination current in silicon diodes, *Solid-State Electron.* 23 (1980) 655–660.
- [17] A. A. Istratov, H. Hieslmair, E. Weber, Iron contamination in silicon technology, *Appl. Phys. A* 70 (2000) 489–534.
- [18] C. W. Pearce, R. G. McMahon, Role of metallic contamination in the formation of "saucer" pit defects in epitaxial silicon, *J. Vac. Sci. Technol.* 14 (1977) 40–43.
- [19] A. Hajjiah, M. Soha, I. Gordon, J. Poortmans, J. John, The impact of interstitial Fe contamination on n-type Cz-Silicon for high efficiency solar cells, *Sol. Energ. Mat. Sol.* 211 (2020) 110550.
- [20] T. T. Le, Z. Zhou, A. Chen, Z. Yang, F. Rougier, D. Macdonald, A. Liu, Reassessing iron–gallium recombination activity in silicon, *J. Appl. Phys.* 135 (2024) 133107.
- [21] M. Maoudj, D. Bouhafs, N. E. Bourouba, A. Hamida-Ferhat, A. El Amrani, Study of the electrical properties of <100> Cz p-type solar-grade silicon wafers against the high-temperature processes, *Appl. Phys. A* 127 (2021) 407.
- [22] O. Olikh, O. Datsenko, S. Kondratenko, Influence of illumination spectrum on dissociation kinetics of iron–boron pairs in silicon, *Phys. Status Solidi A* n/a (2024) 2400351.
- [23] H. S. Laine, V. Vähäniemi, A. E. Morishige, J. Hofstetter, A. Haarahiltunen, B. Lai, H. Savin, D. P. Fenning, Impact of iron precipitation on phosphorus-implanted silicon solar cells, *IEEE Journal of Photovoltaics* 6 (2016) 1094–1102.
- [24] T. Buonassisi, A. A. Istratov, M. D. Pickett, M. Heuer, J. P. Kalejs, G. Hahn, M. A. Marcus, B. Lai, Z. Cai, S. M. Heald, Chemical natures and distributions of metal impurities in multicrystalline silicon materials, *Prog. Photovolt.: Res. Appl.* 14 (2006) 513–531.
- [25] M. D. Abbott, D. Poplavskyy, G. Scardera, D. Inns, F. Lemmi, K. R. McIntosh, S. C. Baker-Finch, Iron contamination in silicon solar cell production environments, in: 2014 IEEE 40th Photovoltaic Specialist Conference (PVSC), pp. 3479–3484.
- [26] M. Schubert, M. Padilla, B. Michl, L. Mundt, J. Giesecke, J. Hohl-Ebinger, J. Benick, W. Warta, M. Tajima, A. Ogura, Iron related solar cell instability: Imaging analysis and impact on cell performance, *Sol. Energy Mater. Sol. Cells* 138 (2015) 96–101.
- [27] A. Herguth, Quantification of iron in boron-doped silicon solar cells from open circuit voltage measurements, *IEEE J. Photovolt.* 12 (2022) 937–947.
- [28] L. Kimerling, J. Benton, Electronically controlled reactions of interstitial iron in silicon, *Physica B+C* 116 (1983) 297–300.
- [29] C. Möller, T. Bartel, F. Gibaja, K. Lauer, Iron–boron pairing kinetics in illuminated p-type and in boron/phosphorus co-doped n-type silicon, *J. Appl. Phys.* 116 (2014) 024503.
- [30] G. Zoth, W. Bergholz, A fast, preparation-free method to detect iron in silicon, *J. Appl. Phys.* 67 (1990) 6764–6771.
- [31] J. Toušek, J. Toušková, A novel approach to the surface photovoltaic method, *Sol. Energy Mater. Sol. Cells* 92 (2008) 1020–1024.
- [32] S. Rein, S. W. Glunz, Electronic properties of interstitial iron and iron–boron pairs determined by means of advanced lifetime spectroscopy, *J. Appl. Phys.* 98 (2005) 113711.
- [33] J. Schmidt, D. Macdonald, Recombination activity of iron–gallium and iron–indium pairs in silicon, *J. Appl. Phys.* 97 (2005) 113712.
- [34] M. Goodarzi, R. A. Sinton, H. Jin, P. Zheng, W. Chen, Q. Wang, D. Macdonald, Accuracy of interstitial iron measurements on p-type multicrystalline silicon blocks by quasi-steady-state photoconductance, *IEEE J. Photovolt.* 7 (2017) 1216–1223.
- [35] O. Olikh, V. Kostylyov, V. Vlasiuk, R. Korkishko, Y. Olikh, R. Chupryna, Features of FeB pair light-induced dissociation and repair in silicon n+p-p+ structures under ultrasound loading, *J. Appl. Phys.* 130 (2021) 235703.
- [36] S. Herlufsen, D. Macdonald, K. Bothe, J. Schmidt, Imaging of the interstitial iron concentration in crystalline silicon by measuring the dissociation rate of iron–boron pairs, *Phys. Status Solidi RRL* 6 (2012) 1–3.
- [37] O. Olikh, Relationship between the ideality factor and the iron concentration in silicon solar cells, *Superlattices Microstruct.* 136 (2019) 106309.
- [38] O. Olikh, O. Lozitsky, O. Zavhorodnii, Estimation for iron contamination in si solar cell by ideality factor: Deep neural network approach, *Prog. Photovoltaics Res. Appl.* 30 (2022) 648–660.
- [39] J. Schmidt, Effect of dissociation of iron–boron pairs in crystalline silicon on solar cell properties, *Progress in Photovoltaics: Research and Applications* 13 (2005) 325–331.
- [40] D. H. Macdonald, L. J. Geerligs, A. Azzizi, Iron detection in crystalline silicon by carrier lifetime measurements for arbitrary injection and doping, *J. Appl. Phys.* 95 (2004) 1021–1028.
- [41] M. A. Green, Improved silicon optical parameters at 25°C, 295 K and 300 K including temperature coefficients, *Prog. Photovoltaics Res. Appl.* 30 (2022) 164–179.
- [42] T. Niewelt, B. Steinhauser, A. Richter, B. Veith-Wolf, A. Fell, B. Hammann, N. Grant, L. Black, J. Tan, A. Youssef, J. Murphy, J. Schmidt, M. Schubert, S. Glunz, Reassessment of the intrinsic bulk recombination in crystalline silicon, *Sol. Energ. Mat. Sol.* 235 (2022) 111467.
- [43] L. E. Black, D. H. Macdonald, On the quantification of Auger recombination in crystalline silicon, *Sol. Energ. Mat. Sol.* 234 (2022) 111428.
- [44] A. Fell, K. R. McIntosh, P. P. Altermatt, G. J. M. Janssen, R. Stangl, A. Ho-Baillie, H. Steinkemper, J. Greulich, M. Müller, B. Min, K. C. Fong, M. Hermle, I. G. Romijn, M. D. Abbott, Input parameters for the simulation of silicon solar cells in 2014, *IEEE J. Photovolt.* 5 (2015) 1250–1263.
- [45] M. Burgelman, P. Nollet, S. Degraeve, Modelling polycrystalline semiconductor solar cells, *Thin Solid Films* 361–362 (2000) 527–532.
- [46] T. K. Joshi, G. Sharma, Y. R. Sharma, A. S. Verma, Spectroscopic screening and performance parameters of hybrid perovskite (CH<sub>3</sub>CH<sub>2</sub>PH<sub>3</sub>PbI<sub>3</sub>) using WIEN2k and SCAPS-1d, *Phys. B Condens. Matter* 682 (2024) 415793.
- [47] B. K. Ravidas, A. Das, S. K. Agnihotri, R. Pandey, J. Madan, M. K. Hossain, M. K. Roy, D. Samajdar, Design principles of crystalline silicon/CsGeI<sub>3</sub> perovskite tandem solar cells using a combination of density functional theory and SCAPS-1D frameworks, *Sol. Energ. Mat. Sol.* 267 (2024) 112688.

- [48] H. Liu, L. Xiang, Q. Liu, P. Gao, Y. Zhang, S. Li, F. Gao, Toward high-performance HTL-free all-perovskite tandem solar cells: SCAPS simulation, *IEEE J. Photovolt.* 14 (2024) 59–64.
- [49] L. You, X. Zhang, Q. Ma, W. Zhu, J. Wu, Optimization of electron transport layer-free Cs<sub>2</sub>TiBr<sub>6</sub>/MASnBr<sub>3</sub> laminated structure perovskite solar cells by SCAPS-1D simulation, *Phys. Status Solidi A* 220 (2023) 2300071.
- [50] A. Ait Abdelkadir, M. Sahal, Theoretical development of the CZTS thin-film solar cell by SCAPS-1D software based on experimental work, *Materials Science and Engineering: B* 296 (2023) 116710.
- [51] J. Liang, Y. Wang, Y. Zhang, X. Liu, J. Lin, Construction of perovskite homojunction for highly efficient perovskite solar cells by SCAPS-1D, *Materials Science and Engineering: B* 301 (2024) 117196.
- [52] M. Abdulmalik, E. Danladi, Influence of perovskite thickness on the performance of silver-doped NaZnBr<sub>3</sub> perovskite solar cells using SCAPS software, *Semiconductor Physics, Quantum Electronics & Optoelectronics* 26 (2023) 321–331.
- [53] R. Pässler, Dispersion-related description of temperature dependencies of band gaps in semiconductors, *Phys. Rev. B* 66 (2002) 085201.
- [54] D. Yan, A. Cuevas, Empirical determination of the energy band gap narrowing in p<sup>+</sup> silicon heavily doped with boron, *J. Appl. Phys.* 116 (2014) 194505.
- [55] R. Couderc, M. Amara, M. Lemiti, Reassessment of the intrinsic carrier density temperature dependence in crystalline silicon, *J. Appl. Phys.* 115 (2014) 093705.
- [56] M. A. Green, Intrinsic concentration, effective densities of states, and effective mass in silicon, *J. Appl. Phys.* 67 (1990) 2944–2954.
- [57] W. O'Mara, R. Herring, L. Hant, *Handbook of semiconductor silicon technology*, Noyes Publications, New Jersey, USA, 1990.
- [58] D. Klaassen, A unified mobility model for device simulation — I. model equations and concentration dependence, *Solid-State Electron.* 35 (1992) 953–959.
- [59] P. P. Altermatt, J. Schmidt, G. Heiser, A. G. Aberle, Assessment and parameterisation of Coulomb-enhanced Auger recombination coefficients in lowly injected crystalline silicon, *J. Appl. Phys.* 82 (1997) 4938–4944.
- [60] W. Wijaranakula, The reaction kinetics of iron–boron pair formation and dissociation in p-type silicon, *J. Electrochem. Soc.* 140 (1993) 275–281.
- [61] J. D. Murphy, K. Bothe, M. Olmo, V. V. Voronkov, R. J. Falster, The effect of oxide precipitates on minority carrier lifetime in p-type silicon, *J. Appl. Phys.* 110 (2011) 053713.
- [62] F. E. Rougiewicz, C. Sun, D. Macdonald, Determining the charge states and capture mechanisms of defects in silicon through accurate recombination analyses: A review, *Sol. Energy Mater. Sol. Cells* 187 (2018) 263 – 272.
- [63] A. A. Istratov, H. Hieslmair, E. Weber, Iron and its complexes in silicon, *Appl. Phys. A: Mater. Sci. Process.* 69 (1999) 13–44.
- [64] B. B. Paudyal, K. R. McIntosh, D. H. Macdonald, Temperature dependent electron and hole capture cross sections of iron-contaminated boron-doped silicon, in: 2009 34th IEEE Photovoltaic Specialists Conference (PVSC), pp. 001588–001593.
- [65] K. Gwozdz, V. Kolkovsky, Fe-related defects in si: Laplace deep-level transient spectroscopy studies, *Phys. Status Solidi A* 219 (2022) 2200139.
- [66] I. Jyothi, V. Janardhanam, H. Hong, C.-J. Choi, Current–voltage and capacitance–voltage characteristics of al schottky contacts to strained si-on-insulator in the wide temperature range, *Mater. Sci. Semicond. Process.* 39 (2015) 390–399.
- [67] C. K. Tang, L. Vines, V. P. Markevich, B. G. Svensson, E. V. Monakhov, Divacancy-iron complexes in silicon, *J. Appl. Phys.* 113 (2013) 044503.
- [68] T. Mcchedlidze, L. Scheffler, J. Weber, M. Herms, J. Neusel, V. Osinniy, C. Moller, K. Lauer, Local detection of deep carrier traps in the pn-junction of silicon solar cells, *Appl. Phys. Lett.* 103 (2013) 013901.
- [69] J. Schön, H. Habenicht, M. C. Schubert, W. Warta, Understanding the distribution of iron in multicrystalline silicon after emitter formation: Theoretical model and experiments, *J. Appl. Phys.* 109 (2011) 063717.
- [70] V. Vähäniemi, A. Haarahiltunen, H. Talvitie, M. Yli-Koski, H. Savin, Impact of phosphorus gettering parameters and initial iron level on silicon solar cell properties, *Progress in Photovoltaics: Research and Applications* 21 (2013) 1127–1135.
- [71] V. Vähäniemi, H. S. Laine, Z. Liu, M. Yli-Koski, A. Haarahiltunen, H. Savin, Full recovery of red zone in p-type high-performance multicrystalline silicon, *Sol. Energ. Mat. Sol.* 173 (2017) 120–127.
- [72] T. Mcchedlidze, C. Möller, K. Lauer, J. Weber, Evolution of iron-containing defects during processing of si solar cells, *J. Appl. Phys.* 116 (2014) 245701.
- [73] O. Olikh, V. Kostylyov, V. Vlasiuk, R. Korkishko, R. Chupryna, Intensification of iron–boron complex association in silicon solar cells under acoustic wave action, *J. Mater. Sci.: Mater. Electron.* 33 (2022) 13133–13142.
- [74] N. Khelfati, H. S. Laine, V. Vähäniemi, H. Savin, F. Z. Bouamama, D. Bouhafs, Dissociation and formation kinetics of iron–boron pairs in silicon after phosphorus implantation gettering, *Phys Status Solidi A* 216 (2019) 1900253.
- [75] D. Yang (Ed.), *Handbook of Photovoltaic Silicon*, Springer Berlin, Heidelberg, first edition, 2019.
- [76] A. McEvoy, T. Markvart, L. Castaner (Eds.), *Solar Cells. Materials, Manufacture and Operation*, Academic Press, Oxford, second edition, 2013.
- [77] A. Goetzberger, J. Knobloch, B. Voss, *Crystalline Silicon Solar Cells*, Wiley, 1998.
- [78] N. Klyui, V. Kostylyov, A. Rozhin, V. Gorbulik, V. Litovchenko, M. Voronkin, N. Zaika, Silicon solar cells with antireflecting and protective coatings based on diamond-like carbon and silicon carbide films, *Opto-Electr. Rev.* 8 (2000) 402–405.
- [79] M. A. Green, Solar cell fill factors: General graph and empirical expressions, *Solid-State Electron.* 24 (1981) 788–789.
- [80] M. A. Green, Accuracy of analytical expressions for solar cell fill factors, *Sol. Cells* 7 (1982) 337–340.
- [81] K. Bothe, D. Hinken, R. Brendel, Extended FF and VOC parameterizations for silicon solar cells, *IEEE J. Photovolt.* 13 (2023) 787–792.
- [82] Y. Srivastava, A. Jain, End-to-end material thermal conductivity prediction through machine learning, *J. Appl. Phys.* 134 (2023) 225101.
- [83] S. Fadhel, C. Delpha, D. Diallo, I. Bahri, A. Migan, M. Trabelsi, M. Mimouni, PV shading fault detection and classification based on I-V curve using principal component analysis: Application to isolated PV system, *Sol. Energy* 179 (2019) 1–10.